materials

MDPI

Article

Two-Stage Sulfuric Acid Leaching of Vanadium-Bearing Carbonaceous Siliceous Ore: Oxidative Pressure Leaching, Kinetics, and Mechanism

Dosmurat Aitkulov [1], Anar Mukhametzhanova [1,2,*], Akmaral Rakhym [2,*] and Aliya Margulanovna Alimzhanova [1]

[1] Republican State Enterprise National Center for Complex Processing of Mineral Raw Materials of the Republic of Kazakhstan, Zhandosov st., 67, Almaty 050036, Kazakhstan; dos.ait.58@mail.ru (D.A.); a.alimzhanova@cmrp.kz (A.M.A.)
[2] Department of Physical Chemistry, Catalysis and Petrochemistry, Faculty of Chemistry and Chemical Technology, Farabi University, Al-Farabi ave., 71, Almaty 050040, Kazakhstan
* Correspondence: narike.91@gmail.com (A.M.); a.rakhym@cmrp.kz (A.R.)

Abstract

Efficient vanadium recovery from carbonaceous siliceous ores is challenging because of the complex mineral occurrence of vanadium and the high chemical resistance of the quartz-rich matrix. In this study, a two-stage processing scheme comprising atmospheric decarbonization–neutralization followed by oxidative autoclave leaching was developed for vanadium-bearing quartzite from the Balasausqandiq deposit (Kyzylorda Region, Kazakhstan). Under the optimized autoclave conditions (140 °C, 120 min, 150 kg t^{-1} H_2SO_4, 5 kg t^{-1} HNO_3, 3 atm O_2, and a solid-to-liquid ratio of 1:1), 88.4% of vanadium was extracted. XRD and SEM–EDS analyses revealed preferential dissolution of reactive V- and Fe-bearing minor phases, while the quartz-rich matrix remained largely preserved, producing a residue containing 72.5 wt.% SiO_2 and <0.01 wt.% carbon. Among the shrinking-core models tested, the product-layer diffusion model provided the closest fit to the available kinetic data (R^2 = 0.9787–0.9865). A three-temperature Arrhenius analysis over 120–140 °C yielded a preliminary apparent activation energy of 54.55 kJ mol^{-1}. Thermodynamic calculations supported the oxidative pathway, showing that V(IV) oxidation by O_2 is favorable at 140 °C ($\Delta_r G^\circ = -75.1$ kJ mol^{-1}). The combined results indicate selective acid–oxidative dissolution of accessible vanadium-bearing phases followed by increasingly restricted extraction from resistant mineral domains within the silica-rich residual matrix. The proposed process integrates efficient vanadium recovery with the generation of a silica-rich residue with potential for use as a secondary metallurgical feedstock, subject to further evaluation.

Keywords: vanadium; vanadium-bearing quartzite; oxidative pressure leaching; sulfuric acid leaching; leaching kinetics; thermodynamic analysis; silica-rich residue

Check for updates

Academic Editor: Hiroaki Onoda

Received: 7 October 2026
Revised: 26 October 2026
Accepted: 1 November 2026
Published: 12 November 2026

Copyright: © 2026 by the authors. Licensee MDPI, Basel, Switzerland. This article is an open access article distributed under the terms and conditions of the Creative Commons Attribution (CC BY) license.

1. Introduction

Vanadium is a strategic metal of increasing importance to modern high-technology industries. Its established use in high-strength low-alloy steels is increasingly complemented by applications in energy-storage technologies, particularly vanadium redox-flow batteries, as well as in the chemical and catalytic industries [1,2]. The major primary and secondary sources of vanadium include titanomagnetite ores, vanadium-bearing slags, stone coal, and black shales [3–5].

Vanadium-bearing carbonaceous–siliceous ores represent a potentially important resource because they may contain vanadium together with other valuable elements, including Ni and Mo [6,7]. However, efficient recovery of vanadium from such materials remains challenging because vanadium is typically incorporated into refractory silicate phases, particularly muscovite and other layered aluminosilicates [8,9]. The structural association of vanadium with the silicate matrix restricts its accessibility to conventional leaching agents and is therefore one of the principal factors controlling extraction efficiency.

A broad range of processing routes has been investigated for vanadium-bearing carbonaceous and shale-type materials, including pyrometallurgical and hydrometallurgical processing, microwave-assisted treatment, mechanochemical activation, and bioleaching. Conventional pyrometallurgical routes generally involve oxidative or salt roasting followed by leaching. Additives such as Na_2CO_3, NaCl, and Na_2SO_4 promote the decomposition of vanadium-bearing minerals and the conversion of vanadium into more soluble forms; however, these processes usually require high temperatures and substantial energy input, while chloride-containing additives may additionally generate chlorine-containing gaseous emissions [4,5]. Incomplete transformation of coarse vanadium-bearing muscovite particles can further limit the efficiency of roasting [10]. Various additives, including MgO [11], $BaCO_3$/CaO [12], and CaF_2/CaO [13], have been proposed to enhance phase transformation and subsequent vanadium leaching. Microwave treatment, mechanochemical activation, and bioleaching have also shown promising results [2,6,10,14,15], although their large-scale implementation may be constrained by specialized equipment requirements, additional pretreatment steps, or relatively slow biochemical kinetics.

In this context, direct hydrometallurgical leaching is attractive as a technologically simpler alternative to routes involving preliminary high-temperature roasting. Eliminating the roasting stage can potentially reduce energy consumption and the number of unit operations while avoiding gaseous emissions associated with salt roasting. Sulfuric acid is among the most extensively investigated reagents for vanadium recovery from low-grade carbonaceous and shale-type materials [16]. Nevertheless, the effectiveness of direct acid leaching remains strongly dependent on the mineralogical occurrence of vanadium. More reactive acid systems have therefore been investigated to destabilize both vanadium-bearing phases and the surrounding silicate matrix. For example, H_2SO_4–HF leaching has been reported to achieve vanadium extraction of up to 96.7% from black shale, followed by the production of V_2O_5 with a purity of 99.52% [17]. These results demonstrate the potential of roasting-free hydrometallurgical processing while also highlighting the need to optimize the leaching chemistry, temperature, and residence time and to establish the kinetic and rate-controlling characteristics of vanadium dissolution.

An additional challenge of hydrometallurgical processing is the generation of substantial quantities of solid leaching residues. These residues are frequently regarded as low-value byproducts and are typically used in construction material applications, despite their potentially useful chemical and mineralogical compositions [2]. Their valorization could reduce the volume of process waste, decrease the consumption of primary mineral resources, and improve the overall resource efficiency of vanadium production. In the case of siliceous vanadium-bearing ores, the selective removal of vanadium and associated minor phases may generate a residue strongly enriched in SiO_2, making it potentially suitable as a secondary raw material for silicon-bearing ferroalloys [18].

Previous studies have demonstrated the feasibility of using leaching residues from vanadium-bearing quartzites as silica-containing components in ferroalloy production. In particular, electric smelting of mixtures containing autoclave leach residue and coal-beneficiation tailings enabled the production of FS45- and FS50-grade ferrosilicon. Thermodynamic modeling predicted silicon recoveries of approximately 70–80% in the temperature

range of 1700–2000 °C, whereas laboratory smelting experiments confirmed the production of FS45 containing 41.1–43.4% Si with a silicon recovery of approximately 79% [19]. Related studies have also shown that more reactive amorphous siliceous materials can enhance silicon recovery during ferrosilicon production [20], whereas the introduction of aluminum enables the production of complex Fe–Si–Al-based alloys with enhanced reducing ability [21]. These observations indicate that silica-rich hydrometallurgical residues should not necessarily be treated as waste but may instead serve as functional components of metallurgical charge materials.

Previous studies have investigated vanadium dissolution kinetics during pressure acid leaching in H_2SO_4–O_2 systems [22] and under non-oxidative conditions [23], demonstrating the influence of reaction conditions and mineral structure on leaching behavior. Xue et al. investigated two-stage pressure acid leaching coupled with lixivium recycling, linking selective vanadium extraction to mineral dissolution and the precipitation of Fe and Al as a kalunite–jarosite solid solution [24]. More recently, Zhao et al. [25] examined vanadium extraction and iron separation in an H_2SO_4–H_3PO_4 system, highlighting the role of solution chemistry and mineral transformations in leaching selectivity. Building on these studies, the present work investigates atmospheric decarbonization–neutralization followed by oxidative autoclave leaching of unroasted quartzite from the Balasausqandiq deposit. Its specific contribution is the combined assessment of vanadium extraction kinetics and changes in the chemical and mineralogical characteristics of the solid residue for this feedstock and process configuration. The potential use of the resulting residue as a secondary silica-bearing feedstock for ferrosilicon production is considered in the context of previous studies, while its metallurgical performance remains to be evaluated.

In the present study, a two-stage processing route comprising atmospheric decarbonization and neutralization followed by oxidative pressure leaching was investigated for vanadium-bearing quartzite from the Balasausqandiq deposit. Vanadium extraction kinetics were evaluated using nonlinear kinetic modeling, including the shrinking-core and Avrami–Erofeyev approaches, and the apparent activation parameters were determined from Arrhenius and Eyring analyses. The chemical and phase compositions of the original ore and the resulting solid residue were characterized to assess the selective removal of vanadium, iron, and other minor mineral phases during leaching. Particular attention was given to silica enrichment in the residue and its implications for potential downstream utilization, although metallurgical performance was not evaluated in this study. This approach combines the assessment of vanadium recovery with residue characterization to identify opportunities for downstream utilization and improved resource efficiency.

2. Materials and Methods

2.1. Materials

Carbonaceous–siliceous quartzites (black shale) from the Balasausqandiq deposit (Greater Karatau, Kyzylorda Region, Kazakhstan) were used as the initial raw material.

The leaching experiments were conducted using technical-grade sulfuric acid (H_2SO_4, 93%, JSC “Base No. 1 of Chemical Reagents”, Moscow, Russia) and nitric acid (HNO_3, 65%, JSC “Base No. 1 of Chemical Reagents”, Moscow, Russia) as the primary reagents. Distilled water was used for the preparation of all solutions and for washing the solid residues. Nitric acid was used as an oxidizing agent during the autoclave leaching stage to promote the oxidation of lower-valence vanadium species, V(III) and V(IV), to the more soluble pentavalent state, V(V).

2.2. Analytical Methods

The morphology and microstructure of the ore and leach residues were examined using a SEM5000 Pro scanning electron microscope (CIQTEK Co., Ltd., Hefei, China) equipped with an Oxford Instruments X-Plore 30 energy-dispersive X-ray spectroscopy (EDS) system incorporating a silicon drift detector (SDD). SEM images were acquired using an InLens detector (CIQTEK Co., Ltd., Hefei, China) at an accelerating voltage of 15 kV. Elemental compositions and spatial distributions were investigated by point EDS analysis and elemental mapping. The quantitative EDS results for the leach residue are reported as the mean ± standard deviation of measurements at 12 locations on a single specimen. These statistics describe spatial compositional heterogeneity within the specimen rather than variability between independent leaching experiments.

X-ray fluorescence semiquantitative analysis was performed using an Axios 1 kW X-ray fluorescence wavelength-dispersive spectrometer (PANalytical, Almelo, The Netherlands). The obtained data were processed and interpreted in SuperQ software (Omnian 37).

X-ray diffraction measurements were performed using a MiniFlex diffractometer (Rigaku, Tokyo, Japan) equipped with a D/teX Ultra detector (Rigaku, Tokyo, Japan), operated at 40 kV and 15 mA. Diffraction patterns were collected in continuous θ–2θ scanning mode over a 2θ range of 3–90°, with a step size of 0.02° and a scanning speed of 10° min^{-1}. Crystalline phases were identified using the ICDD PDF-2 database (Release 2016). Quantitative phase analysis was performed using the reference intensity ratio (RIR) method. Phase contents were normalized to the sum of the identified crystalline phases. Minor-phase abundances were treated as semiquantitative because of their low concentrations and overlapping diffraction peaks.

The concentrations of V, Fe, Al, and Si in the leach solutions were determined by inductively coupled plasma optical emission spectrometry (ICP-OES; iCAP 6500, Thermo Scientific, Waltham, MA, USA). Before analysis, the solutions were filtered through a 0.45 μm membrane filter and diluted as required. Calibration was performed using multi-element standard solutions over a concentration range of 0.1–100 mg L^{-1}, yielding coefficients of determination (R^2) greater than 0.999. The detection limits were 0.01 mg L^{-1} for V, 0.005 mg L^{-1} for Fe, 0.02 mg L^{-1} for Al, and 0.03 mg L^{-1} for Si. Each leaching condition was tested once, without independent experimental replicates. The ICP-OES analytical RSD, determined from five replicate measurements of standard solutions, did not exceed 2%; this value does not represent the overall uncertainty of the leaching experiments.

The relative standard deviation, calculated from five replicate measurements of standard solutions, did not exceed 2%.

Vanadium speciation in the leach solutions, specifically the relative occurrence of V(IV) and V(V), was monitored by potentiometric titration. The pH and oxidation–reduction potential (ORP) of the solutions were measured using calibrated electrodes.

The total carbon and sulfur contents of the ore and leach residues were determined by combustion analysis using a CHNS analyzer (ELTRA, Haan, Germany). A weighed sample (approximately 0.05–0.2 g) was combusted in an oxygen atmosphere at 1350 °C. Carbon and sulfur were detected as CO_2 and SO_2, respectively, by infrared absorption, and their contents were determined by calibration with certified reference materials.

2.3. Ore Preparation

The as-received ore, with a maximum particle size of 25 mm, was initially crushed in a jaw crusher (FLSmidth, Copenhagen, Denmark) to a particle size less than 1 mm and subsequently sieved through a 0.2 mm sieve (Figure 1). The oversize fraction was further ground in a dry rod mill (FLSmidth, Copenhagen, Denmark) for 20 min. After preparation, 75% of the particles were smaller than 45 μm, and the specific surface area of the material

ranged from 12.5 to 18.3 m^2 g^{-1}. The resulting <0.2 mm fraction was used in the subsequent leaching experiments.



(**a**) (**b**)

Figure 1. Initial ore and ore preparation process: (**a**) carbonaceous–siliceous quartzite (black shale) from the Balasausqandiq deposit; (**b**) ore preparation procedure.

2.4. Sulfuric Acid Leaching (LSB-HAL) Experiments

2.4.1. Atmospheric Leaching Experiments (Stage I)

Owing to the high carbonate and chloride contents of the ore, a separate decarbonization–neutralization stage was introduced prior to autoclave leaching. The combined pregnant leach solution and wash solutions were heated to 90 °C and contacted with fresh ore at solid-to-liquid (S:L) ratios ranging from 1:1.1 to 1:4 for 60 min under continuous stirring. This stage facilitated the neutralization of residual sulfuric acid, increasing the pH from 0.4–0.5 to 0.8–1.2, and the decomposition of residual carbonate phases. The resulting partially neutralized solution was suitable for subsequent ion-exchange recovery of vanadium and uranium, whereas the neutralized solid residue was directed to the autoclave leaching stage.

Laboratory-scale atmospheric leaching experiments were conducted in a 5000 mL glass reactor equipped with a mechanical stirrer operated at 400 rpm and a thermostatic temperature-control system with an accuracy of ±1 °C. The S:L ratio was varied from 1:3 to 1:6 (g mL^{-1}), while the H_2SO_4 concentration ranged from 50 to 200 g L^{-1}. The leaching time was varied between 2 and 8 h. At the end of each experiment, the slurry was filtered through filter paper, and the solid residue was washed with distilled water until a neutral filtrate was obtained and subsequently dried at 105 °C. The concentrations of V, Fe, Al, and Si in the resulting solutions were determined by inductively coupled plasma-optical emission spectrometry (ICP-OES).

The decarbonization–neutralization process was subsequently carried out on an enlarged scale using a custom-built 65 dm^3 stainless-steel reactor operated under continuous mechanical agitation. The working volume corresponded to approximately 80% of the total reactor capacity. A slurry was prepared by mixing the ore with the pregnant solution obtained from autoclave leaching at an S:L ratio of 1:2 and was introduced into the reactor through the loading port. After loading, the reactor was closed, and the slurry was heated to 90 °C.

The enlarged-scale decarbonization–neutralization stage was conducted for 120 min at 90 °C, while the slurry pH was maintained below 1.3–1.5. The selected temperature range of approximately 85–95 °C corresponded to the practical operating range under atmospheric-pressure conditions; temperatures below 85 °C resulted in less effective interactions between

the residual acid and the solid material. During this stage, residual acidity was consumed through interactions with the fresh ore and carbonate-containing phases.

Upon completion of the process, the hot slurry was discharged at approximately 90 °C and subjected to vacuum filtration. The pregnant filtrate, containing the dissolved metals transferred into solution during processing, including V, U, Mo, Fe, and Al, was collected in storage vessels for subsequent downstream processing. The resulting solid residue was transferred to the slurry-preparation vessel and subsequently used as the feed material for the autoclave leaching stage.

Vacuum filtration was performed for approximately 3 h using a cylindrical AISI 316 stainless-steel vacuum filter (INOKS LLP, Almaty, Kazakhstan) equipped with a removable filter-cloth retaining element, receiver, and vacuum pump. The filtration unit was mounted on a mobile platform. Following solid–liquid separation, the filtrate was transferred to storage vessels for further processing, whereas the recovered cake was used to prepare the slurry for subsequent autoclave leaching.

2.4.2. Autoclave Leaching Experiments (Stage II)

Laboratory-scale autoclave leaching experiments were conducted in a 7 L autoclave (Premex, Lyss, Switzerland) (Figure 2). A 2500 g portion of the solid material was used in each experiment at a solid-to-liquid (S:L) ratio of 1:1. Concentrated H_2SO_4 and HNO_3 were added at dosages of 150 and 5 kg t^{-1} of solid feed, respectively. Oxygen was supplied to an initial pressure of 3 atm. The leaching process was carried out at 140 °C for 120 min under continuous agitation.



Figure 2. Laboratory-scale autoclave leaching setup.

The autoclave leaching process was subsequently performed on an enlarged scale in a 65 dm^3 stainless-steel reactor under continuous mechanical agitation. A slurry was prepared using the solid residue obtained after Stage I atmospheric treatment, water, sulfuric acid, and nitric acid. The dosages of concentrated H_2SO_4 and HNO_3 were maintained at 150 and 5 kg t^{-1} of solid feed, respectively, and the S:L ratio was 1:1. The prepared slurry was introduced into the reactor through the loading port, after which the reactor was tightly sealed and heated. The autoclave leaching stage was conducted at 140 °C for 120 min.

The reactor and the associated Nutsche filtration unit used for the enlarged-scale experiments are schematically illustrated in Figure 3. An enlarged version of Figure 3 is

provided in the Supplementary Materials as Figures S1 and S2, presented in landscape format across two pages for improved readability.

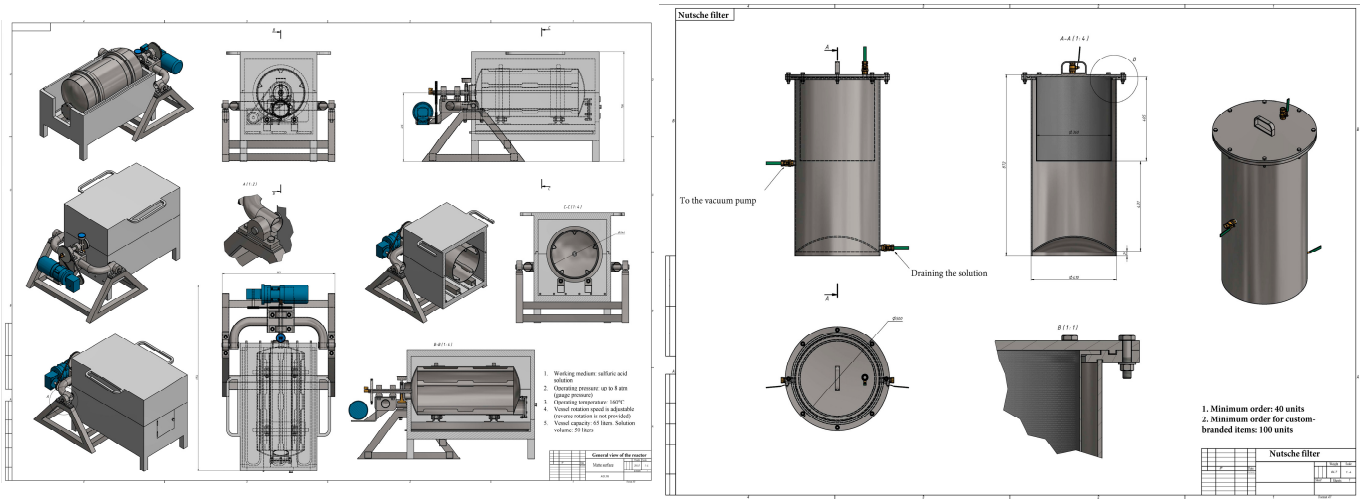

(**a**) (**b**)

Figure 3. Schematic representation of the reactor and Nutsche filtration system: (**a**) reactor; (**b**) Nutsche filter.

After the autoclave leaching stage was completed, the reactor was cooled from 140 °C to approximately 90–95 °C before depressurization. Once the required temperature was reached, the residual pressure was carefully released, and the hot slurry was discharged into the vacuum filtration unit (Figure 4a,b). Solid–liquid separation was performed at approximately 90–95 °C, with a filtration time of approximately 2 h.

The resulting pregnant leach solution was collected in storage vessels and subsequently recycled for slurry preparation in the Stage I atmospheric treatment. The solid leaching residue was subjected to two-stage washing with hot water, and the resulting wash solutions were also recycled for atmospheric-stage slurry preparation. The washed solid residue was subsequently dried in an oven at 105 °C.

This solution-recycling configuration enabled the pregnant autoclave leach solution and wash liquors to be reused during the atmospheric decarbonization–neutralization stage, while the solid residue from Stage I was returned as feed to the autoclave leaching stage.

After the autoclave leaching process was complete, the reactor was cooled from 140 °C to approximately 90–95 °C prior to depressurization. Cooling was initiated after the reactor heating system was switched off and, when needed, was accelerated by directing an external airflow from a fan onto the reactor body. Once the temperature had decreased to 90–95 °C, the residual pressure inside the reactor was gradually released.

The hot slurry was subsequently discharged at 90–95 °C and transferred to the vacuum filtration unit (Figure 4c,d). Filtration was carried out for approximately 2 h. The resulting pregnant leach solution was collected in storage vessels and subsequently recycled for preparation of the slurry used in the atmospheric leaching stage. The solid residue (leach cake) was subjected to two-stage washing with hot water and subsequently dried in an oven at 105 °C.

Each leaching experiment was performed as a single run unless otherwise indicated.



Figure 4. Enlarged-scale experimental setup and filtration process: (**a**) autoclave reactor coupled with a vacuum filtration unit; (**b**) Nutsche filter; (**c**) vacuum filtration of the slurry after autoclave leaching; and (**d**) filtered cake.

2.5. Integrated Hydrometallurgical Processing Flowsheet

The processing of vanadium-bearing quartzite from the Balasausqandiq deposit is based on a two-stage sulfuric acid leaching process involving oxidative treatment with oxygen and nitric acid as a cyclic oxidizing agent (Figure 5). The proposed flowsheet comprises the following main stages: ore preparation (grinding), decarbonization–neutralization under atmospheric conditions, oxidative autoclave leaching, and filtration with separation into a pregnant leach solution and a solid residue (sludge flux). The proposed downstream routes include recovery of vanadium concentrates from the pregnant leach solution and potential utilization of the solid residue in ferroalloy production. Electric smelting of the residue was not evaluated in the present study.

The decarbonization–neutralization step is an essential pretreatment stage that reduces acid consumption and provides suitable conditions for subsequent autoclave leaching. During the autoclave stage, the introduction of O_2 promotes the oxidation of vanadium to V(V) and facilitates the oxidative dissolution of vanadium-bearing sulfide phases, including iron divanadium(III) sulfide (FeV_2S_4) and copper vanadium sulfide. Under the optimized experimental conditions, the overall vanadium extraction reached approximately 85%.

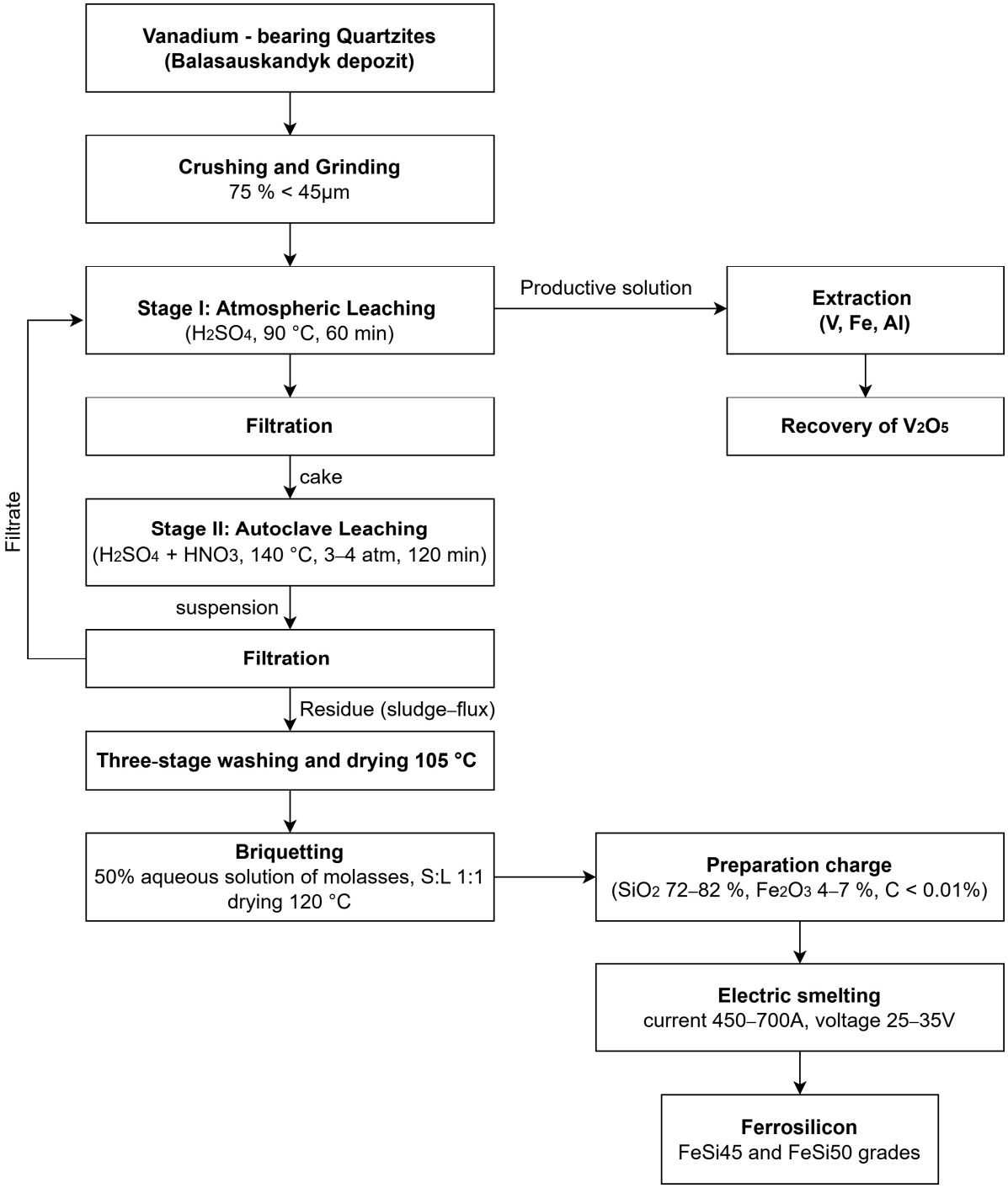

Figure 5. Proposed integrated processing flowsheet for vanadium-bearing quartzite from the Balasausqandiq deposit, combining vanadium recovery with ferroalloy production from the hydrometallurgical residue.

The proposed integrated flowsheet for processing vanadium-bearing quartzite from the Balasausqandiq deposit is presented in Figure 5. The chemical reactions underlying the leaching process and their thermodynamic interpretation are discussed in Section 3.5. The process includes crushing and grinding of the ore to obtain a material in which 75% of the particles are smaller than 45 μm, followed by atmospheric sulfuric acid leaching at 90 °C for 60 min and subsequent solid–liquid separation by filtration.

The resulting pregnant leach solution is directed to the recovery of vanadium, iron, and aluminum, followed by the production of V_2O_5. The solid residue obtained after the

atmospheric stage is subsequently subjected to autoclave leaching in the presence of H_2SO_4 and HNO_3 at 140 °C for 120 min. Following filtration, the solid residue is washed, dried, mixed with a molasses solution, and briquetted.

Electric smelting is proposed as a possible downstream route for utilizing the residue as a secondary silica-bearing feedstock for ferrosilicon production. Its metallurgical performance requires validation through dedicated smelting tests.

2.6. Theory and Calculations

2.6.1. Kinetic Modelling Methodology

The kinetics of vanadium leaching were analyzed using the experimental extraction data obtained at 120, 130, 140, and 150 °C. The extraction fraction (α) was calculated as follows:

$$\alpha = \frac{m_t}{m_0}, \quad (1)$$

where m_t is the amount of vanadium leached at time t and m_0 is the initial amount of vanadium in the ore. m_t was calculated as:

$$m_t = C_{V,t} D_t V_t \quad (2)$$

where $C_{V,t}$ is the vanadium concentration measured by ICP-OES in the diluted analytical sample (g L^{-1}), D_t is the dilution factor, and is the leach solution volume (L).

To investigate the rate-controlling mechanism of the leaching process, the experimental data were fitted using four kinetic models based on the shrinking-core model (SCM) [26,27], namely, the external film diffusion model, chemical reaction control model, product-layer diffusion model, and mixed-control model, together with the Avrami–Erofeyev equation [28].

The corresponding kinetic equations are given below:

External film diffusion

$$\alpha = k_f t \quad (3)$$

Chemical reaction control

$$1 - (1 - \alpha)^{1/3} = k_r t \quad (4)$$

Product-layer diffusion control

$$1 - \frac{2}{3}\alpha - (1 - \alpha)^{2/3} = k_d t \quad (5)$$

Mixed control

$$(1 - \alpha)^{-1/3} - 1 + \frac{1}{3}\ln(1 - \alpha) = k_m t \quad (6)$$

Avrami–Erofeyev model

$$-\ln(1 - \alpha) = k t^n \quad (7)$$

where k_f, k_r, k_d, and k_m are the apparent rate constants of the corresponding kinetic models, while k and n are the kinetic parameters of the Avrami–Erofeyev equation.

The kinetic parameters were determined by direct nonlinear least-squares fitting of the experimental extraction curves using the original extraction fraction without linear transformation. For the product-layer diffusion and mixed-control models, the extraction fraction was obtained by numerical solution of the corresponding implicit equations for each trial value of the rate constant.

The goodness of fit was evaluated using the coefficient of determination (R^2) (Equation (8)), root mean square error (RMSE) (Equation (9)), adjusted root mean

square error ($RMSE_{adj}$) (Equation (10)), and average absolute relative deviation (AARD) (Equation (11)):

$$R^2 = 1 - \frac{\sum\left(\alpha_{exp} - \alpha_{calc}\right)^2}{\sum\left(\alpha_{exp} - \bar{\alpha}_{exp}\right)^2} \quad (8)$$

$$RMSE = \sqrt{\frac{1}{N}\sum(\alpha_{exp} - \alpha_{calc})^2} \quad (9)$$

$$RMSE_{adj} = \sqrt{\frac{\sum(\alpha_{exp} - \alpha_{calc})^2}{N - p}} \quad (10)$$

$$AARD(\%) = \frac{100}{N}\sum\left|\frac{\alpha_{exp} - \alpha_{calc}}{\alpha_{exp}}\right| \quad (11)$$

where N is the number of experimental observations and p is the number of fitted parameters.

2.6.2. Activation Energy Calculation

The apparent activation energy of vanadium leaching was determined using the Arrhenius equation on the basis of the apparent rate constants obtained from the best-performing mechanistic kinetic model. The linear form of the Arrhenius equation is expressed as follows:

$$\ln k = \ln A - \frac{E_a}{RT}, \quad (12)$$

where k is the apparent rate constant, A is the preexponential factor, E_a is the apparent activation energy (J mol^{-1}), R is the universal gas constant (8.314 J mol^{-1} K^{-1}), and T is the absolute temperature (K).

The activation energy was calculated from the slope of the linear dependence of lnk versus 1/T:

$$E_a = -\text{slope} \times R. \quad (13)$$

The Arrhenius regression was restricted to the three apparent rate constants obtained at 120, 130, and 140 °C, because the value at 150 °C departed from the increasing temperature trend. This restricted-range analysis provides a preliminary, model-dependent estimate of the apparent activation energy rather than establishing Arrhenius behavior over the full investigated temperature range.

2.6.3. Thermodynamic Activation Parameters

The thermodynamic activation parameters of the leaching process were evaluated according to transition-state theory using the Eyring equation [29]:

$$k = \frac{k_B T}{h}\exp\left(\frac{\Delta S^{\ddagger}}{R}\right)\exp\left(-\frac{\Delta H^{\ddagger}}{RT}\right), \quad (14)$$

where k_B is the Boltzmann constant (1.380649×10^{-23} J K^{-1}), h is Planck's constant ($6.62607015 \times 10^{-34}$ J s), $\Delta H^{\ddagger}$ is the activation enthalpy, and $\Delta S^{\ddagger}$ is the activation entropy.

The linearized form of the Eyring equation is

$$\ln\left(\frac{k}{T}\right) = -\frac{\Delta H^{\ddagger}}{R}\left(\frac{1}{T}\right) + \ln\left(\frac{k_B}{h}\right) + \frac{\Delta S^{\ddagger}}{R}. \quad (15)$$

The activation enthalpy was obtained from the slope of the linear regression according to

$$\Delta H^{\ddagger} = -\text{slope} \times R, \quad (16)$$

whereas the activation entropy was calculated from the intercept:

$$\Delta S^{\ddagger} = R\left[\text{intercept} - \ln\left(\frac{k_B}{h}\right)\right]. \quad (17)$$

The Gibbs free energy of activation at each experimental temperature was subsequently calculated using

$$\Delta G^{\ddagger} = \Delta H^{\ddagger} - T\Delta S^{\ddagger}. \quad (18)$$

The Eyring regression used the same three temperature-dependent rate constants as the Arrhenius analysis. The resulting parameters are treated as apparent descriptors of the fitted overall leaching rate, rather than activation parameters of an identified elementary reaction.

3. Results and Discussion

3.1. Characterization of the Original Ore

Efficient recovery of valuable components from black shale ores strongly depends on the technological parameters of ore preparation, among which the particle size of the ground material is one of the key factors [30].

Table 1 presents the chemical composition of the initial vanadium-bearing ore from the Balasausqandiq deposit. The ore is predominantly composed of SiO_2, which accounts for 68.39 wt.%, and contains approximately 12 wt.% carbon and 0.67–0.80 wt.% V_2O_5.

Table 1. Chemical composition of the initial ore.

Mass Fractions of the Determined Elements, wt.%								
SiO_2	CaO	MgO	TiO_2	V_2O_5	P	Al_2O_3	Fe	Mo
68.39	0.96	0.31	0.90	0.67–0.80	0.31	2.94	1.93	0.23
Na	K	Cu	Pb	Zn	Total S	Cd	W	Bi
0.14	0.29	0.04	0.009	0.004	1.0	<0.01	0.06	<0.01
Ni	Co	Mn	As	U	C			
0.02	<0.01	0.008	0.06	0.01	12			

Other major and minor constituents include Al_2O_3 (2.94 wt.%), Fe (1.93 wt.%), S (1.0 wt.%), P (0.31 wt.%), and molybdenum oxide (0.23 wt.%), together with smaller amounts of Ca, Mg, Ti, Na, K, Cu, Pb, Zn, W, Ni, Co, Mn, As, and U.

The high SiO_2 content confirms the predominantly siliceous nature of the ore, whereas the presence of carbon, iron, aluminum, sulfur, and other minor components reflects its complex polymineralic composition. The V_2O_5 content of 0.67–0.80 wt.% confirms the potential value of the material as a vanadium-bearing resource. The relatively high carbon content provides a rationale for introducing a preliminary decarbonization stage, while the occurrence of vanadium- and iron-bearing phases supports the use of subsequent oxidative sulfuric acid leaching to promote vanadium dissolution.

Mineralogical analysis of the initial vanadium-bearing quartzite ore from the Balasausqandiq deposit revealed the presence of iron hydroxides ($(HFeO)_2$) and pyrite (FeS_2) as the major ore minerals.

The iron hydroxides exhibited heterogeneous coloration ranging from light gray to dark gray, low reflectivity, and relatively high hardness. The minerals showed both isotropic and anisotropic optical behavior and were characterized by red internal reflections, which facilitated their identification among the other mineral phases. In the initial ore, iron hydroxides occurred predominantly as anhedral grains with a characteristic size of approximately 113.4 μm (Figure 6).

Pyrite identified in the sample was characterized by a yellow color and high reflectivity. It crystallized in the cubic system and displayed isotropic optical properties. Pyrite occurred as relatively rare anhedral grains with irregular, locally curved boundaries. The size of individual liberated pyrite grains reached 3.5–21.4 µm (Figure 6).

The X-ray diffraction pattern of the initial ore (Figure 7) is characterized by a pronounced predominance of the quartz phase. According to the results of the quantitative phase analysis, quartz accounts for 96.70% of the crystalline phases, whereas the remaining components are minor phases, including illite-2M2 (0.38%), vanadian-barian muscovite-2M1 (0.60%), iron phosphate hydroxide (0.70%), iron divanadium(III) sulfide (0.50%), katoite (0.55%), copper vanadium sulfide (0.30%), and barium silicon oxide (0.35%).

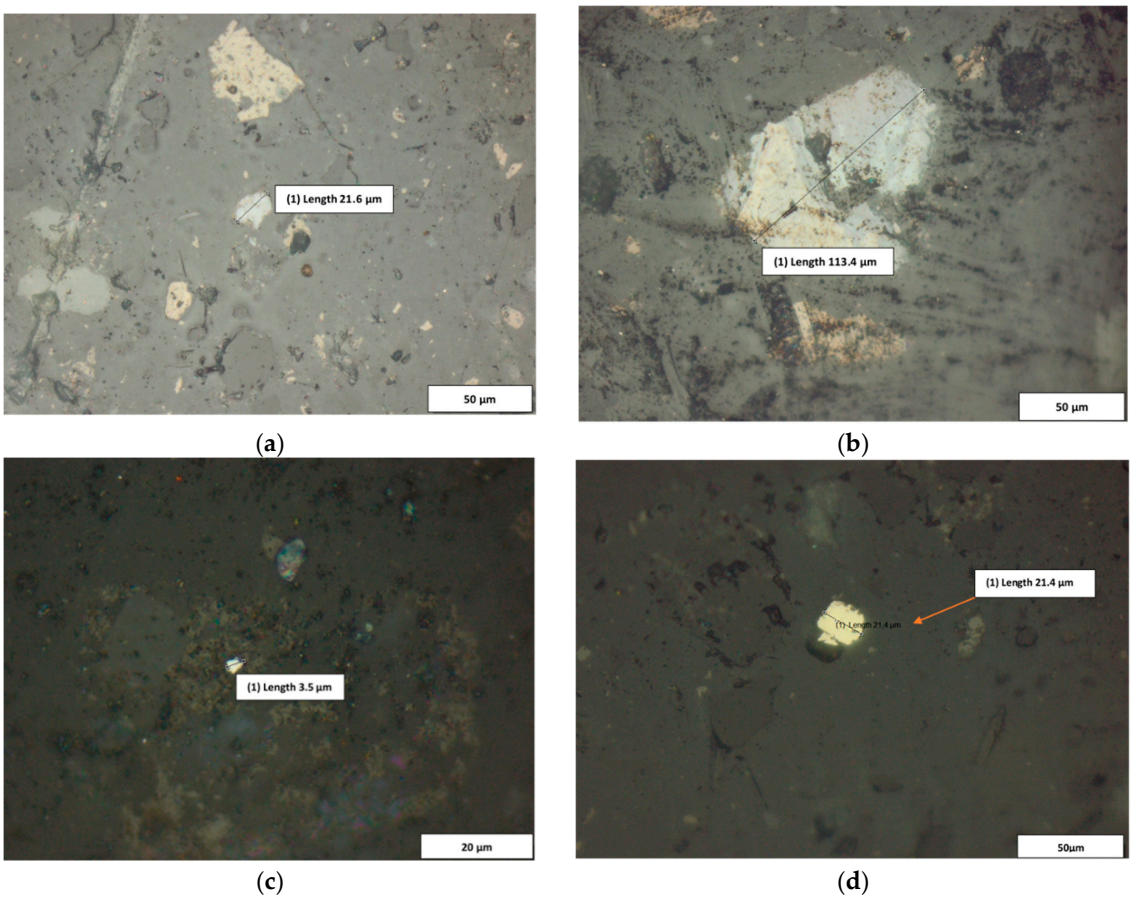

Figure 6. (**a**,**b**) Iron hydroxides; (**c**,**d**) pyrite.

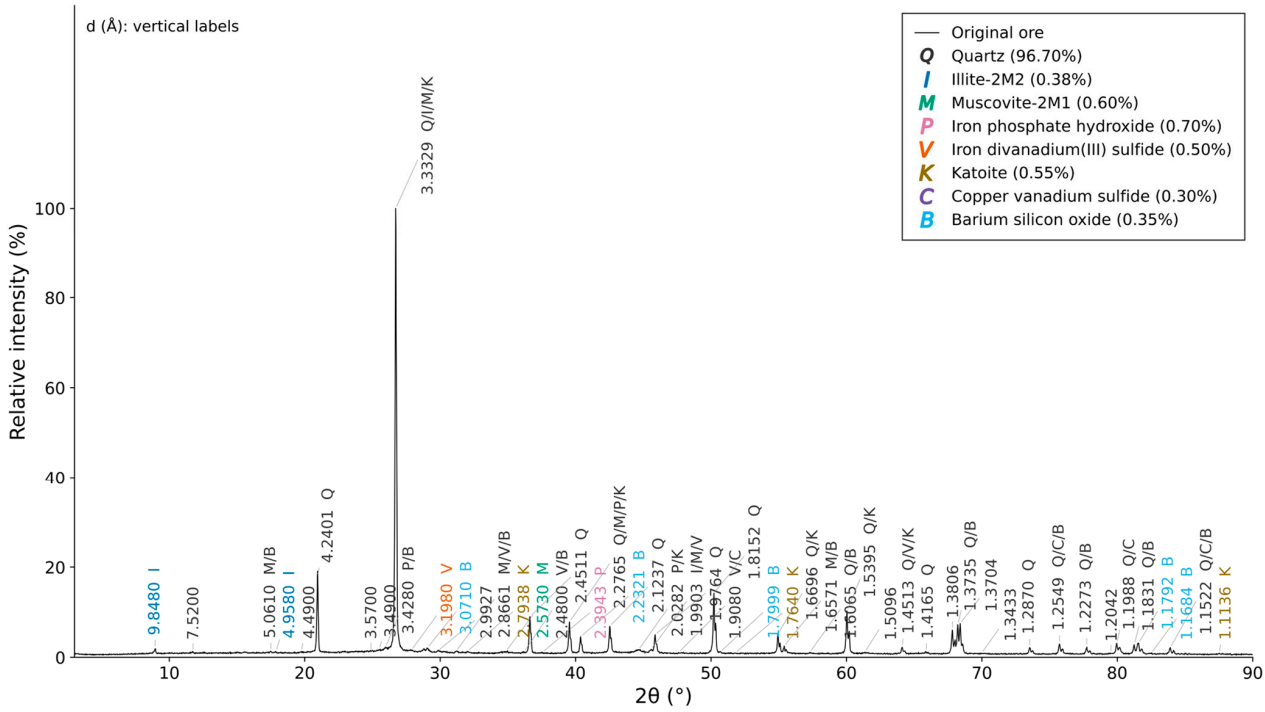

Figure 7. X-ray diffraction pattern of the initial vanadium-bearing quartzite ore from the Balasausqandiq deposit.

The major intense reflections at 2θ = 20.934° and 26.726°, corresponding to interplanar spacings of d = 4.2401 and 3.3329 Å, respectively, were assigned to quartz. The reflection at 2θ = 26.726° exhibited the highest intensity and was located in a region where reflections attributed to quartz, illite, muscovite, and katoite overlap [31]. Additional quartz reflections were observed at 2θ = 36.632° (d = 2.4511 Å), 39.555° (d = 2.2765 Å), 40.375° (d = 2.2321 Å), 42.533° (d = 2.1237 Å), 50.219° (d = 1.8152 Å), 54.949° (d = 1.6696 Å), and 60.045° (d = 1.5395 Å), as well as in the higher-angle region.

The low-angle reflection at 2θ = 8.972°, corresponding to an interplanar spacing of d = 9.848 Å, was associated with the basal reflections of illite and muscovite [32]. The peaks at 2θ = 17.51–17.88° may also include contributions from layered aluminosilicate phases and iron divanadium(III) sulfide [31]. Reflections in the regions of 2θ = 27–29°, 34–37°, 42–48°, and 54–60° partially overlap with diffraction lines assigned to katoite, iron phosphate hydroxide, and vanadium-bearing sulfide phases. In particular, the reflections at approximately 2θ = 42.53° and 45.5–45.9° may contain contributions from iron divanadium(III) sulfide, muscovite, and iron phosphate hydroxide.

Overall, the initial ore is characterized by a predominantly quartz-rich matrix containing minor amounts of layered aluminosilicates, calcium aluminate, iron phosphate, and vanadium-bearing sulfide phases.

Microstructural analysis of the sample revealed distinct morphological and optical characteristics of the iron hydroxides and pyrite, providing a basis for their identification and further characterization as ore minerals in the initial material.

SEM images of the initial vanadium-bearing quartzite at different magnifications are shown in Figure 8a,b. The sample exhibits a heterogeneous morphology consisting of irregular angular and subangular particles of different sizes. Relatively large compact fragments coexist with numerous finer particles attached to their surfaces and filling the interparticle spaces. The higher-magnification image (Figure 8b) further reveals rough and irregular particle surfaces, indicating a structurally heterogeneous mineral material.

The local elemental composition of the initial ore was evaluated by EDS analysis at 12 representative points distributed over the sample surface (Figure S3a), and the averaged results are summarized in Table S1. The point analyses were dominated by O and Si, with mean contents of 46.86 ± 8.87 wt.% and 42.85 ± 14.37 wt.%, respectively, confirming the predominantly siliceous character of the material. Considerably lower average contents were determined for Fe (2.78 ± 4.88 wt.%), Al (2.13 ± 3.01 wt.%), S (2.04 ± 4.02 wt.%), K (1.31 ± 1.78 wt.%), V (0.83 ± 1.14 wt.%), and Ba (0.62 ± 1.11 wt.%), while Ca, Mg, Cr, Ti, and Ni were detected only in minor amounts. The relatively high standard deviations, particularly for Si, Fe, Al, S, and V, indicate pronounced variations in the local chemical composition between individual analysis points. A representative EDS spectrum obtained at point 10 is presented in Figure S1b and shows intense Si and O signals together with weaker contributions from Al, K, V, Fe, Ba, Ca, Cr, and Ni. These point-analysis results characterize the local microscale composition of the ore and complement the bulk chemical composition determined by XRF.

Since vanadium is the target element of the present study, its spatial distribution was additionally examined by EDS elemental mapping. Individual Si (Figure 8e) and Fe (Figure 8f) maps are also presented to facilitate visual comparison of the elemental distributions. These maps provide complementary qualitative information on the Si-rich matrix and the distribution of Fe-bearing constituents; however, visual comparison alone does not establish their association with vanadium. The V Kα1 map shown in Figure 8d provides a qualitative visualization of the weak vanadium signal within the analyzed area. However, the low signal intensity and the absence of count-resolved mapping data limit reliable assessment of spatial variations and do not allow distinct V-rich domains to be confidently identified or excluded. The map alone therefore cannot establish whether vanadium occurs in finely dispersed phases or determine its association with the quartz-rich matrix. The relatively low average V concentration obtained from the point EDS analyses and the XRD identification of minor vanadium-bearing crystalline phases support the presence of vanadium in the initial ore but do not independently establish its spatial distribution.

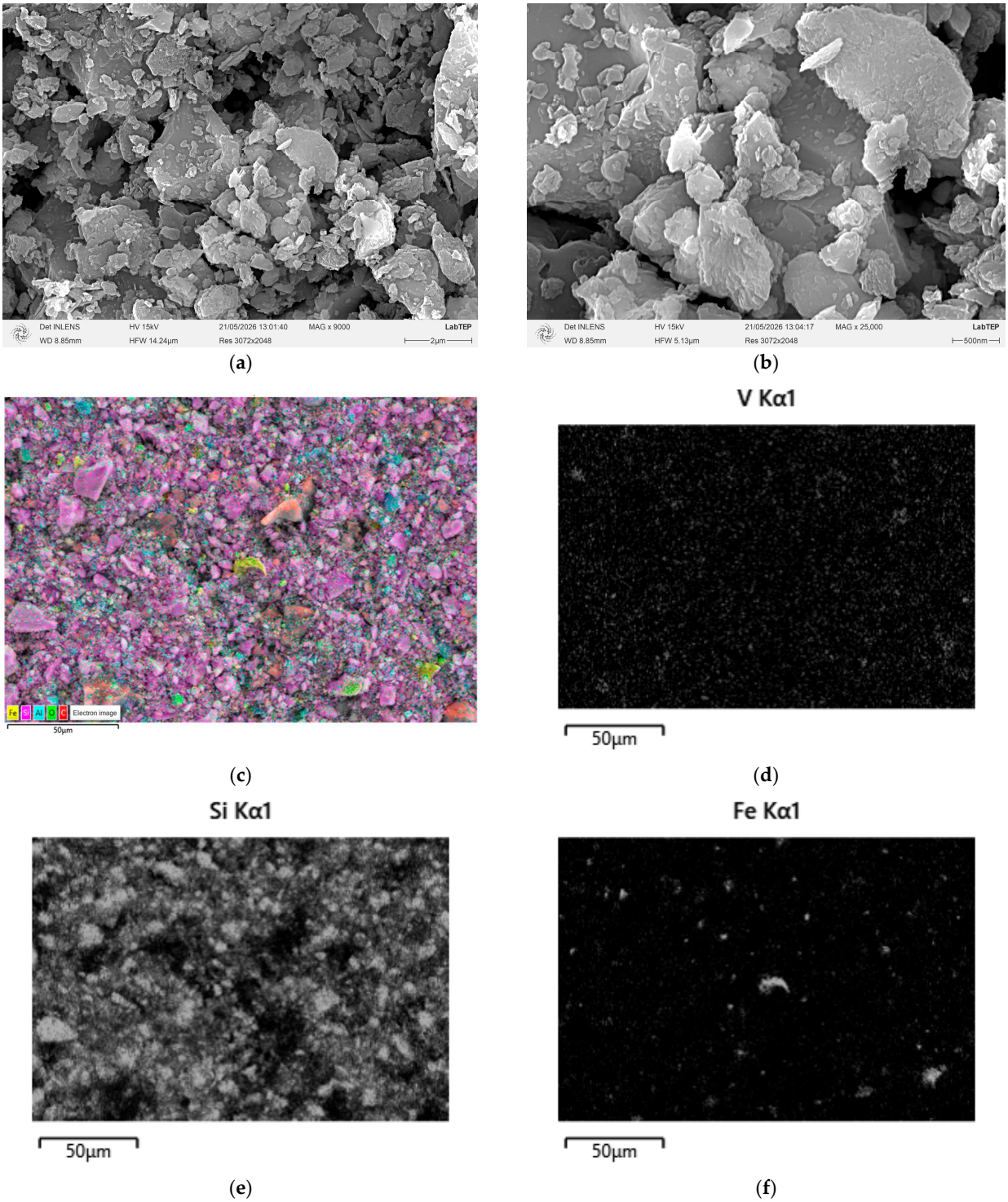

Figure 8. SEM–EDS characterization of the initial vanadium-bearing quartzite from the Balasausqandiq deposit: (**a**,**b**) SEM images at different magnifications; (**c**) overlaid EDS elemental distribution map; (**d**) EDS elemental distribution map of vanadium (V Kα1); (**e**) EDS elemental distribution map of silicon (Si Kα1); (**f**) EDS elemental distribution map of iron (Fe Kα1).

3.2. Optimization of Sulfuric Acid Leaching Conditions

3.2.1. Stage I: Decarbonization–Neutralization Under Atmospheric Pressure

Table 2 presents the results of an investigation into the effects of key technological parameters on vanadium extraction during atmospheric leaching.

Table 2. Effect of technological parameters on vanadium extraction during atmospheric leaching.

Temperature, °C	Leaching Time, min	S:L Ratio	V Extraction, %	Optimal Condition	Interpretation
80	60	1:2	62.4	90 ± 5 °C	A plateau in V extraction is observed at 90–95 °C
85			72.8		
90			79.6		
95			80.1		
100			79.4		
90	30	1:2	62.0	60 min	Further increase in V extraction after 60 min is marginal
	45		72.5		
	60		79.5		
	75		80.2		
	90		80.0		
90	60	1:1	74.2	1:2	Increasing the liquid fraction beyond an S:L ratio of 1:2 does not improve V extraction
		1:1.5	77.5		
		1:2	79.5		
		1:2.5	78.7		
		1:3	76.9		

The effects of temperature, atmospheric leaching time, and the solid-to-liquid (S:L) ratio on vanadium extraction were investigated (Table 2). Increasing the temperature from 80 to 90 °C resulted in an increase in vanadium extraction from 62.4 to 79.6%. At 95 °C, the extraction reached 80.1%, whereas a further increase in temperature to 100 °C resulted in a slight decrease to 79.4%, indicating that no substantial improvement was achieved at higher temperatures. Therefore, 90 ± 5 °C was selected as the operating temperature range.

Increasing the leaching time from 30 to 60 min increased vanadium extraction from 62.0 to 79.5%. Further extension of the process to 75 and 90 min produced only marginal changes, with extraction values of 80.2 and 80.0%, respectively. Accordingly, a leaching time of 60 min was selected as the operating condition.

The S:L ratio also affected vanadium extraction. Increasing the S:L ratio from 1:1 to 1:2 increased the extraction from 74.2 to 79.5%. A further increase in the liquid fraction, corresponding to S:L ratios of 1:2.5 and 1:3, resulted in slight decreases in extraction to 78.7 and 76.9%, respectively. Therefore, an S:L ratio of 1:2 was selected.

On the basis of these results, the operating conditions selected for the atmospheric leaching stage were 90 ± 5 °C, 60 min, and an S:L ratio of 1:2.

3.2.2. Stage II: Autoclave Oxidative Leaching

Table 3 presents the results of the investigation into the effects of technological parameters on vanadium extraction during autoclave leaching.

Table 3. Effect of technological parameters on vanadium extraction during autoclave leaching.

Temperature, °C	Leaching Time, min	H_2SO_4, kg/t	HNO_3, kg/t	O_2 Overpressure, atm	S:L Ratio	V Extraction, %	Optimal Condition	Interpretation
120	120	150	5	3	1:1	72.0	140 °C	V extraction decreases at 150 °C; therefore, a further increase in temperature is not beneficial
130						83.0		
140						88.4		
150						86.8		
140	30	150	5	3	1:1	68.5	120 min	No appreciable increase in V extraction is observed beyond 120 min
	60					80.8		
	90					87.6		
	120					88.4		
	180					88.2		
140	120	100	5	3	1:1	76.5	150 kg/t	Excess H_2SO_4 above 150 kg/t does not improve V extraction
		125				82.1		
		150				88.4		
		175				88.0		
		200				86.7		
140	120	150	0	3	1:1	77.2	5 kg/t	A further increase in HNO_3 dosage provides no technological benefit
			2.5			83.8		
			5			88.4		
			7.5			88.0		
			10			86.9		
140	120	150	5	0	1:1	72.5	3 atm	V extraction reaches a plateau at an O_2 overpressure of 3 atm
				1		79.0		
				2		84.6		
				3		88.4		
				4		88.0		
140	120	150	5	3	1:0.8	84.8	1:1	Increasing the liquid fraction decreases the vanadium concentration without improving extraction
					1:1	88.4		
					1:1.2	87.7		
					1:1.5	85.9		

The effects of temperature, leaching time, sulfuric and nitric acid dosages, oxygen overpressure, and the solid-to-liquid (S:L) ratio were evaluated. On the basis of the experimental results, operating conditions providing the highest vanadium extraction under rational technological parameters were selected.

Increasing the temperature from 120 to 140 °C increased vanadium extraction from 72.0 to 88.4%. A further increase in temperature to 150 °C resulted in a decrease in extraction to 86.8%, indicating that further temperature elevation was not technologically justified. Therefore, 140 °C was selected as the optimal temperature.

Vanadium extraction decreased slightly from 88.4% at 140 °C to 86.8% at 150 °C. This small difference should be interpreted cautiously because its statistical significance has not been established. One possible contributing factor is increased diffusional resistance within the silica-rich residual matrix, consistent with the product-layer diffusion model discussed in Section 3.4. However, the available data do not establish temperature-dependent changes in the structure or permeability of this matrix. Thus, 140 °C was selected as the preferred operating temperature within the investigated range, as increasing the temperature to 150 °C provided no improvement in extraction [22].

Increasing the autoclave leaching time from 30 to 120 min resulted in an increase in vanadium extraction from 68.5 to 88.4%. Extending the treatment time to 180 min produced virtually no further improvement, with an extraction of 88.2%. Accordingly, a process duration of 120 min was selected as the optimal condition, since prolonged treatment did not result in any appreciable increase in vanadium extraction.

Increasing the sulfuric acid dosage from 100 to 150 kg/t increased vanadium extraction from 76.5 to 88.4%. Further increases in H_2SO_4 dosage to 175 and 200 kg/t resulted in extraction values of 88.0 and 86.7%, respectively. On the basis of these results, an H_2SO_4 dosage of 150 kg/t was selected as the optimal condition.

The addition of nitric acid also had a pronounced effect on vanadium extraction. Increasing the HNO_3 dosage from 0 to 5 kg/t increased the extraction from 77.2 to 88.4%. Further increases to 7.5 and 10 kg/t did not improve the process efficiency, with extraction decreasing to 88.0 and 86.9%, respectively. Therefore, an HNO_3 dosage of 5 kg/t was selected as the optimal condition.

Increasing the oxygen overpressure from 0 to 3 atm increased vanadium extraction from 72.5 to 88.4%. A further increase to 4 atm resulted in a slight decrease in extraction to 88.0%.

It should be noted that even at zero O_2 overpressure, substantial vanadium extraction (72.5%) was still observed. A possible explanation is that the nitric acid dosage (5 kg t^{-1}) was maintained in all experiments, and HNO_3 can act as an independent oxidant, promoting the oxidation of lower-valence vanadium species to V(V). Acid dissolution of accessible vanadium-bearing phases may also contribute, without necessarily requiring complete oxidation of vanadium to V(V). The increase in extraction from 72.5 to 88.4% with increasing O_2 overpressure is consistent with an additional oxidant supply that promotes oxidative dissolution and helps maintain oxidizing conditions in the pulp. A similar role of nitric acid as an oxidizing agent in sulfuric acid leaching of vanadium-bearing ores has been reported previously [16].

Thus, an oxygen overpressure of 3 atm was considered sufficient to reach a plateau in the oxidative effect and was selected as the operating condition.

The S:L ratio also affected vanadium extraction. Changing the ratio from 1:0.8 to 1:1 increased extraction from 84.8 to 88.4%. A further increase in the liquid fraction to S:L ratios of 1:1.2 and 1:1.5 decreased vanadium extraction to 87.7 and 85.9%, respectively. Therefore, an S:L ratio of 1:1 was selected as the optimal condition.

Overall, the optimal conditions for autoclave leaching were determined to be a temperature of 140 °C, a leaching time of 120 min, an H_2SO_4 dosage of 150 kg/t, an HNO_3 dosage of 5 kg/t, an oxygen overpressure of 3 atm, and an S:L ratio of 1:1. These conditions were adopted for the second oxidative stage of the integrated processing scheme for the vanadium-bearing black shale ore.

Validation experiments performed under comparable conditions resulted in pregnant leach solutions containing 3.4–3.5 g/L total vanadium, of which 1.73–1.94 g/L was present as V(V), when using a 1 L reactor. In the 7 L reactor, the concentrations of total vanadium and V(V) reached 5.8 and 2.2 g/L, respectively, with the oxidation–reduction potential (ORP) ranging from 780 to 805 mV.

3.2.3. Overall Process Parameters

A two-stage countercurrent leaching regime was developed through a series of consecutive laboratory experiments involving stepwise optimization of reagent dosages and operating conditions. The optimized process parameters are summarized in Table 4.

Table 4. Optimized operating parameters of the two-stage leaching process.

Parameter	Stage I—Atmospheric Leaching	Stage II—Autoclave Leaching
Temperature, °C	90	140
H_2SO_4 dosage, kg/t	–	150
HNO_3 dosage, kg/t	–	5
O_2 overpressure, atm	–	3
S:L ratio	1:2	1:1
Leaching time, min	60	120
pH of the pregnant leach solution	0.8–1.2	0.4–0.5
ORP of the pregnant leach solution, mV	440–660	700–805

3.3. Characterization of the Sludge Flux

The solid residue (sludge flux) obtained after the two-stage leaching process (Figure 9) was characterized by a high silica content and a low residual total carbon content.



Figure 9. Solid residue (sludge flux) obtained after two-stage leaching under laboratory conditions.

The chemical composition of the sludge flux obtained after autoclave leaching of black shale ore from the Balasausqandiq deposit is presented in Table 5.

Table 5. Chemical composition of the sludge flux obtained after autoclave leaching of black shale ore from the Balasausqandiq deposit.

Mass Fractions of the Determined Elements, wt.%								
SiO_2	CaO	MgO	TiO_2	V_2O_5	P	Al_2O_3	Fe	Mo
72.5	0.94	0.24	0.55	0.1	<0.01	1.25	0.99	0.02
Na	K	Cu	Pb	Zn	Total S	Cd	W	Bi
0.093	0.056	0.008	0.008	0.002	0.95	<0.01	0.05	<0.01
Ni	Co	Mn	As	U	C			
0.017	<0.01	0.005	<0.01	0.001				

The substantial removal of carbon, from 12.6% in the initial ore to <0.01% in the leach residue, together with the high SiO_2 content (72.5%), suggests the potential use of the resulting sludge flux as a silica-bearing feedstock for ferrosilicon production. Previous

studies on related leaching residues provide a basis for considering this application [19,20]. However, the smelting performance of the residue produced under the present leaching conditions was not evaluated in this study.

After leaching, the positions of the major quartz XRD reflections remained essentially unchanged (Figure 10). The most intense reflection was retained at 2θ = 26.719° (d = 3.3337 Å), compared with 2θ = 26.726° (d = 3.3329 Å) for the initial ore. Similarly, the low-angle quartz reflection shifted only slightly from 2θ = 20.934° (d = 4.2401 Å) to 2θ = 20.946° (d = 4.2377 Å). The preservation of the reflections at 2θ = 36.323°, 39.541°, 40.370°, 42.529°, 50.217°, 54.951°, 60.034°, and 64.115°, as well as those in the higher-angle region, indicates that the crystalline structure of the quartz matrix was not substantially altered during leaching [31].

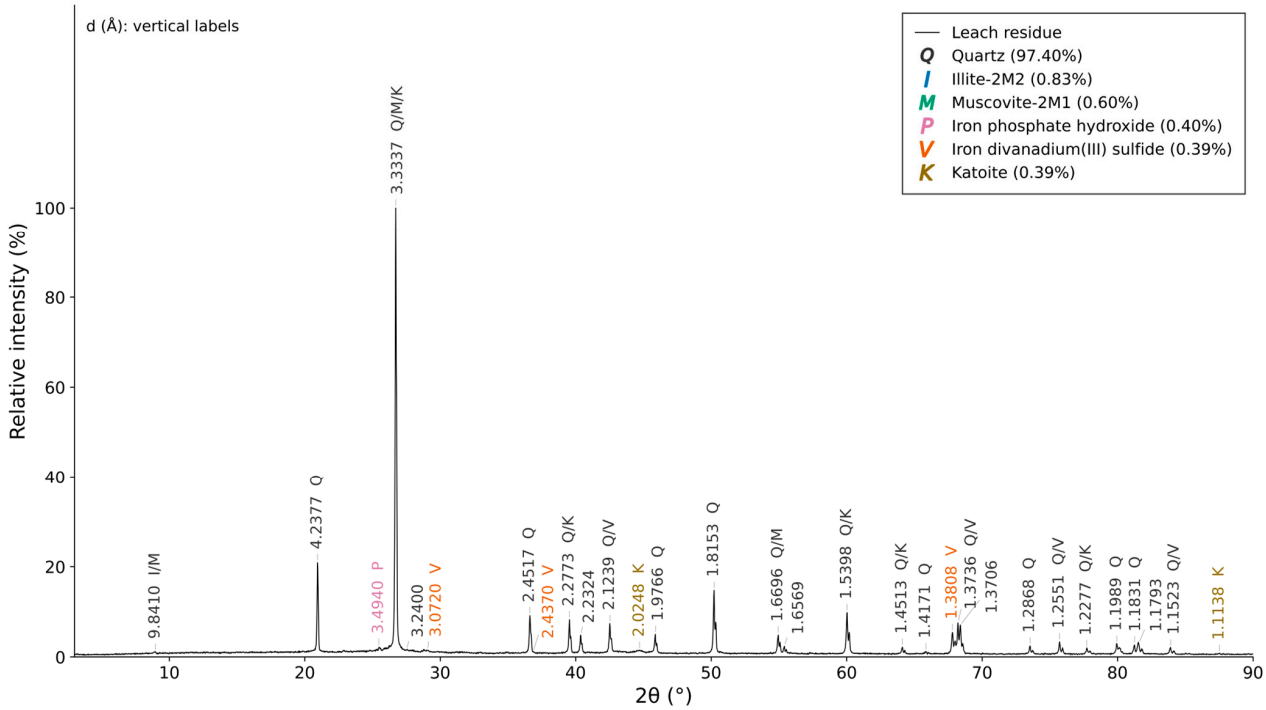

Figure 10. XRD pattern of the sludge flux obtained after two-stage leaching under laboratory conditions.

Quantitative phase analysis revealed an increase in the relative quartz content from 96.70 to 97.40%. This change is unlikely to result from the formation of additional quartz and can instead be attributed to the relative enrichment of the solid residue in silica following the partial dissolution of less stable minor phases.

The relative content of illite-2M2 increased from 0.38 to 0.83%, whereas the muscovite content remained essentially unchanged at 0.60% before and after leaching. The low-angle reflection at 2θ = 8.979° (d = 9.841 Å), associated with the basal reflections of illite and muscovite, was retained after leaching. The apparent increase in the illite fraction is therefore more reasonably interpreted as the relative enrichment of this persistent layered phase in the solid residue rather than its formation during leaching. Given its low abundance, however, peak overlap and uncertainties associated with quantitative phase analysis may also contribute to the observed difference [32].

The content of iron phosphate hydroxide decreased from 0.70 to 0.40% after leaching. Its presence is indicated, in particular, by the reflection at 2θ = 36.85° (d = 2.437 Å), together with possible contributions to the reflections at 2θ = 39.541° and 44.72. The decrease in the relative abundance of this phase suggests its partial dissolution under the applied leaching conditions [33,34].

The relative content of iron divanadium(III) sulfide decreased from 0.50 to 0.39%. Its reflections overlap with those of quartz at approximately 2θ = 42.53°, 45.87°, and 54.95° and at higher diffraction angles; therefore, changes in this minor phase are evaluated from the combined set of matching reflections rather than from a single isolated peak. The decrease in the calculated FeV_2S_4 content is consistent with the partial transfer of iron and vanadium from the solid phase into the leach solution.

The katoite content decreased from 0.55 to 0.39%. Its contribution may occur within the major overlapping reflection at approximately 2θ = 26.72°, as well as near 2θ = 40.37°, 50.22°, 68.39°, and 79.95°. In addition, copper vanadium sulfide and barium silicon oxide, which accounted for 0.30 and 0.35%, respectively, of the initial ore, were no longer identified in the quantitative phase composition after leaching. This may indicate their preferential dissolution during treatment or a decrease in their abundance below the reliable detection limit of powder X-ray diffraction [33,34].

Overall, the XRD results indicate that leaching did not substantially disrupt the dominant quartz structure but was accompanied by the partial removal of Fe-, V-, Cu-, Ba-, and Ca-bearing minor phases. Consequently, a silica-rich solid residue enriched in quartz formed, while small amounts of relatively persistent layered aluminosilicate phases remained. Because the individual minor phases occur at concentrations less than approximately 1%, changes in their calculated abundances should be regarded as semiquantitative, particularly in regions characterized by extensive peak overlap and the limited accuracy of quantitative XRD analysis for trace crystalline phases [31].

SEM images of the solid residue obtained after two-stage leaching are shown in Figure 11a,b. The residue retains the heterogeneous particulate morphology observed for the initial ore (Figure 8a,b), consisting of irregular angular and subangular particles with a broad size distribution. Relatively large compact fragments coexist with numerous finer particles, while their surfaces remain rough and locally covered with smaller adhered fragments. Thus, although the two-stage acid treatment substantially alters the chemical and phase composition of the material [16], no pronounced homogenization of the particle morphology is observed at the investigated scale.

The local elemental composition of the residue was evaluated by SEM–EDS point analysis at 12 representative locations (Figure S4a), and the averaged results are summarized in Table S2.

Si and O remained the predominant elements, with mean contents of 46.70 ± 11.51 wt.% Si and 40.25 ± 18.93 wt.% O, respectively. For comparison, the corresponding values for the initial ore were 42.85 ± 14.37 wt.% Si and 46.86 ± 8.87 wt.% O (Table S1). The increase in the mean Si content after leaching is consistent with the relative enrichment of the solid residue in the silica-rich component following dissolution and removal of more acid-reactive mineral constituents. This observation also agrees with the XRD results, which revealed an increase in the relative quartz content from 96.70 to 97.40% after leaching.

Changes were also observed for the minor elements. The average Fe content decreased from 2.78 ± 4.88 wt.% in the initial ore to 1.97 ± 3.71 wt.% in the residue, whereas Al decreased from 2.13 ± 3.01 to 1.76 ± 3.84 wt.% and K decreased from 1.31 ± 1.78 to 1.09 ± 2.65 wt.%. These changes are consistent with the partial removal of Fe-bearing and aluminosilicate-associated components during acid leaching, although the high standard deviations indicate substantial point-to-point variability and therefore preclude direct quantitative assessment of elemental extraction based solely on EDS data. In contrast, the mean S content increased from 2.04 ± 4.02 to 6.85 ± 18.01 wt.%. This apparent increase is strongly influenced by a small number of locally S-rich particles and should therefore be interpreted as evidence of heterogeneous residual sulfur-bearing domains rather than bulk sulfur enrichment.

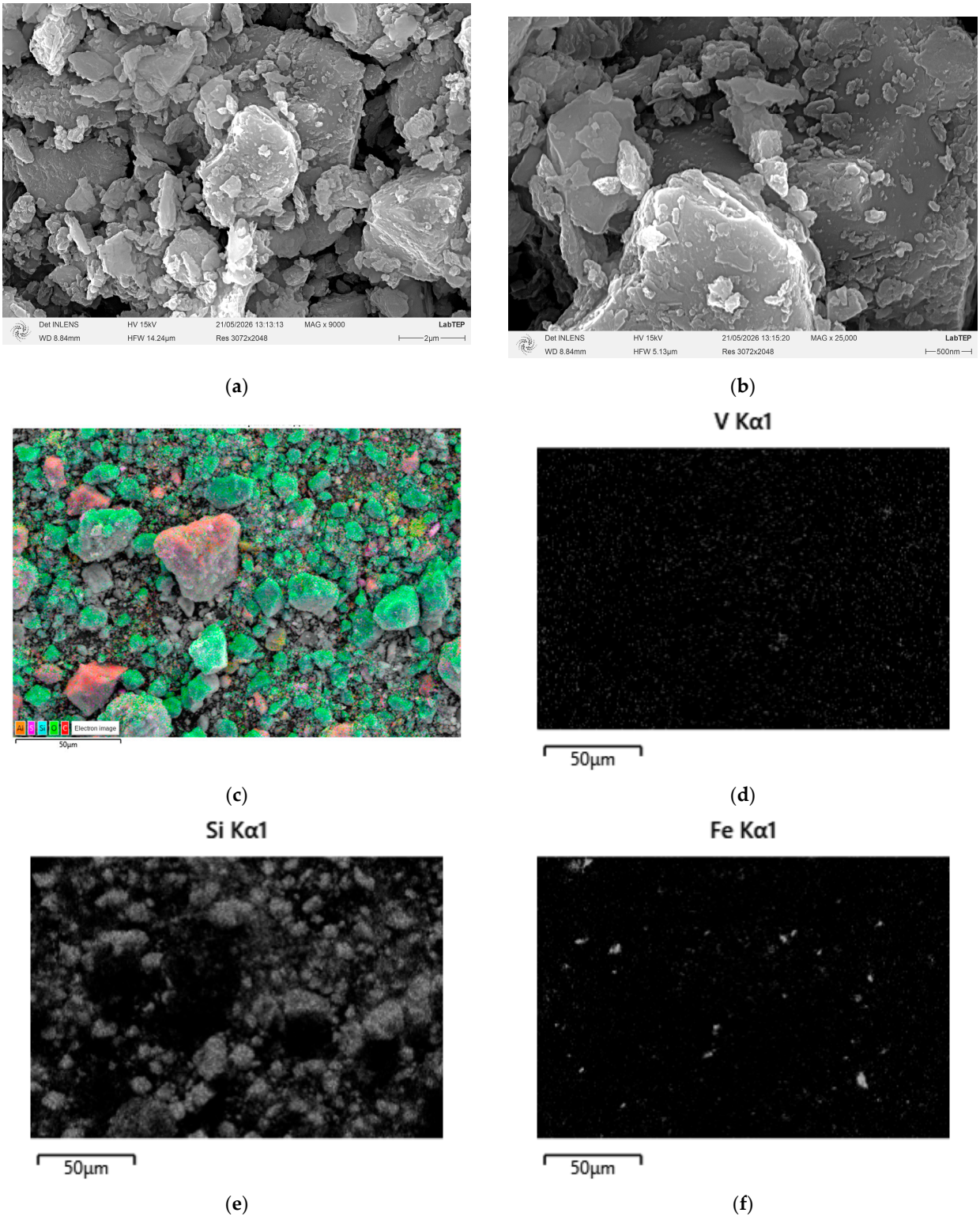

Figure 11. SEM–EDS characterization of the sludge flux obtained after two-stage leaching of the vanadium-bearing quartzite from the Balasausqandiq deposit: (**a**,**b**) SEM images at different magnifications; (**c**) overlaid EDS elemental distribution map; (**d**) EDS elemental distribution map of vanadium (V Kα1); (**e**) EDS elemental distribution map of silicon (Si Kα1); (**f**) EDS elemental distribution map of iron (Fe Kα1).

Particular attention was given to vanadium because it is the target element of the leaching process. The mean V content determined by point EDS was 0.83 ± 1.14 wt.% in the initial ore and 0.68 ± 1.67 wt.% in the leached residue. The substantial variability among

measurement locations prevents these mean values from being interpreted as evidence of a statistically established decrease in V content. The large standard deviations indicate considerable spatial variability in the point EDS results. However, the weak V signal and the absence of count-resolved mapping data limit interpretation of the V Kα1 map (Figure 11d). The map is therefore treated as a qualitative illustration and does not independently establish the presence or persistence of locally V-enriched domains after leaching.

Overall, a comparison of the initial ore and the leached residue indicates that the two-stage treatment results in relative enrichment of the solid phase in Si, accompanied by partial removal of Fe-, Al-, K-, and V-bearing constituents. Moreover, SEM–EDS mapping and point analyses reveal that the remaining vanadium is not uniformly retained but occurs in localized multicomponent domains. These microscale observations complement the XRD results showing preservation and relative enrichment of the quartz matrix together with a decrease or disappearance of several minor Fe-, V-, Cu-, Ba-, and Ca-bearing crystalline phases after leaching.

3.4. Vanadium Leaching Kinetics

The kinetic data analyzed in this section were obtained from autoclave leaching experiments conducted at different temperatures and leaching times, with the H_2SO_4 dosage, HNO_3 dosage, O_2 overpressure, and solid-to-liquid ratio held constant at 150 kg t^{-1}, 5 kg t^{-1}, 3 atm, and 1:1, respectively.

The kinetic curves of vanadium extraction during autoclave sulfuric acid leaching at 120–150 °C are shown in Figure 12. Increasing the temperature from 120 to 140 °C markedly accelerated vanadium dissolution. After 15 min, the extraction efficiencies were 28.5, 36.8, 45.2, and 42.6% at 120, 130, 140, and 150 °C, respectively, whereas after 90 min, they reached 70.2, 81.3, 87.6, and 85.4%, respectively. The highest extraction was therefore obtained at 140 °C, while a further increase to 150 °C provided no additional improvement. Vanadium dissolution was most rapid during the initial stage of leaching and gradually slowed with time, with the kinetic curves approaching a plateau after approximately 90 min. Accordingly, the data obtained at 15, 30, 60, and 90 min were used for kinetic modeling, whereas the 120- and 180-min points were excluded because they corresponded to the near-plateau region.

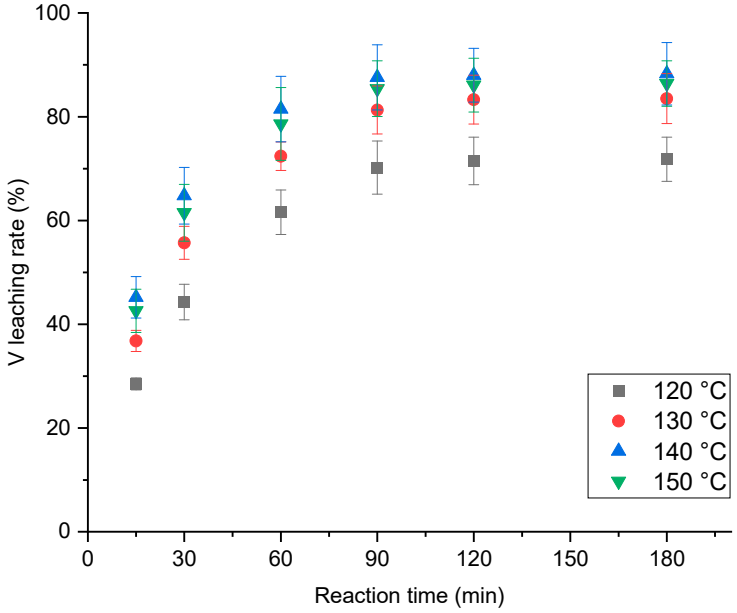

Figure 12. Kinetic curves of V autoclave leaching at different temperatures.

The experimental data within the kinetically active region were fitted using the models described in Section 2.6. The resulting kinetic parameters and goodness-of-fit criteria are summarized in Table 6, while the corresponding nonlinear fitting curves are presented in Figures S5–S9.

Table 6. Results of kinetic model fitting.

Model	T (°C)	k_d	n	R^2	RMSE	AARD (%)
Film diffusion	120	0.009178	-	0.327	0.1522	29.45
	130	0.010826	-	−0.107	0.2064	31.92
	140	0.012005	-	−0.915	0.2630	34.89
	150	0.011607	-	−0.629	0.2443	34.06
Chemical reaction	120	0.004589	-	0.760	0.0909	16.41
	130	0.006468	-	0.718	0.1042	15.82
	140	0.009202	-	0.700	0.1041	12.48
	150	0.008079	-	0.680	0.1083	14.31
Product-layer diffusion	120	0.000932	-	0.9787	0.0271	4.81
	130	0.001478	-	0.9862	0.0230	3.59
	140	0.002089	-	0.9827	0.0250	3.06
	150	0.001859	-	0.9865	0.0222	3.05
Mixed control	120	0.000781	-	0.905	0.0571	11.04
	130	0.001436	-	0.897	0.0629	9.25
	140	0.002326	-	0.897	0.0609	7.45
	150	0.001976	-	0.902	0.0599	7.85
Avrami–Erofeyev	120	0.05104	0.7099	0.99669	0.01307	2.03
	130	0.06864	0.7154	0.99669	0.01382	1.65
	140	0.09080	0.7086	0.99583	0.01503	1.56
	150	0.08509	0.7026	0.99667	0.01353	1.49

Note: For the shrinking-core models, k_d is expressed in min^{-1}. For the Avrami–Erofeyev model, k_d has units of min^{-n} according to the equation.

The film-diffusion model showed the poorest agreement with the experimental data, with R^2 values ranging from −0.915 to 0.327 and AARD values ranging from 29.45–34.89%. The negative R^2 values obtained at 130–150 °C further indicate that external mass transfer through the liquid film does not adequately describe the observed kinetics. The chemical-reaction model provided a better fit (R^2 = 0.680–0.760; AARD = 12.48–16.41%), while the mixed-control model showed a further improvement (R^2 = 0.897–0.905; AARD = 7.45–11.04%). Nevertheless, both models remained clearly inferior to the product-layer diffusion model.

The kinetic analysis was based on four sampling times per temperature (15, 30, 60, and 90 min), without independent replicate leaching experiments. This limited dataset restricts model discrimination and parameter precision, particularly for models containing two fitted parameters. The reported R^2, RMSE, and AARD values therefore describe agreement with the available observations rather than providing independent validation of a rate-controlling mechanism. Numerical solution of the implicit model equations does not remove this limitation. Accordingly, the product-layer diffusion model is regarded as a candidate description consistent with the observed leaching behavior, rather than definitive evidence of exclusive diffusion control. Additional early-stage measurements and independent

experimental replicates are required for more reliable model discrimination and uncertainty estimation.

Among the mechanistically interpretable shrinking-core expressions, the product-layer diffusion model provided the best description of the experimental kinetics. The R^2 values remained within 0.9787–0.9865, while the RMSE and AARD were limited to 0.0222–0.0271 and 3.05–4.81%, respectively. The apparent rate constant, k_d, increased from 0.000932 min^{-1} at 120 °C to 0.001478 min^{-1} at 130 °C and 0.002089 min^{-1} at 140 °C. At 150 °C, k_d decreased slightly to 0.001859 min^{-1}, which is consistent with the absence of any further increase in vanadium extraction above 140 °C.

Shevko et al. [19] reported that the behavior of silica plays a significant role in the leaching kinetics of vanadium-containing quartzites under atmospheric-pressure conditions, and the kinetics may be governed predominantly by diffusion through the progressively developing product layer, which is consistent with the results obtained in this work. Despite the generally low reactivity of SiO_2 in dilute acidic media, partial disruption of the silicate framework may be accompanied by the formation of amorphous hydrated silica ($SiO_2 \cdot nH_2O$), which can form a dense gel-like layer on the particle surface. This layer acts as a diffusion barrier, hindering acid transport toward the unreacted core and restricting the outward transport of reaction products.

The Avrami–Erofeyev equation yielded the best overall statistical fit to the experimental conversion curves, with R^2 = 0.9958–0.9967, RMSE = 0.0131–0.0154, and AARD = 1.49–2.03%. The Avrami exponent remained nearly constant over the investigated temperature range (n = 0.7026–0.7154), indicating similar conversion curve characteristics at all temperatures. However, the superior statistical performance of the Avrami–Erofeyev model should not be interpreted as direct evidence of a specific nucleation-and-growth mechanism [35]. Rather, in the present heterogeneous mineral system, the model is best regarded as an empirical representation of the overall solid-phase conversion behavior.

Accordingly, the Avrami–Erofeyev equation was retained as the best empirical description of the kinetic curves, whereas the product-layer diffusion model was selected as the best-performing mechanistically interpretable SCM expression. Because the kinetic fitting was based on four data points per temperature, the mechanistic interpretation should be regarded as tentative, and additional measurements in the early stage of leaching would improve model discrimination and parameter precision [36].

The apparent activation energy was estimated using the rate constants obtained from the product-layer diffusion model at 120, 130, and 140 °C (Figure 13). The 150 °C value was excluded because it departed from the increasing temperature trend. With three observations and two fitted regression coefficients, the Arrhenius fit has only one residual degree of freedom. Consequently, the high R^2 should be interpreted cautiously and does not establish the robustness of the slope or validate a specific mechanism. The estimated activation energy applies only to the selected temperature interval and kinetic model.

The resulting Arrhenius relationship was as follows:

$$\ln k_d = -6.5613\left(\frac{1}{T}\right) + 5.6320 \quad (19)$$

with R^2 = 0.9954 (Figure 13), yielding a preliminary estimate of the apparent activation energy of E_a = 54.55 kJ mol^{-1}.

The obtained value indicates a pronounced temperature dependence of the apparent leaching rate within the investigated linear range. However, the magnitude of the apparent activation energy alone is insufficient to identify a specific rate-controlling mechanism [35] and is therefore considered here primarily as a quantitative measure of the temperature sensitivity of the process.

To complement the Arrhenius analysis, the temperature dependence of k_d was further evaluated using the Eyring transition-state equation to estimate the apparent activation enthalpy, entropy, and Gibbs free energy (Figure 14). Consistent with the Arrhenius analysis, only the linear temperature range of 120–140 °C was considered.

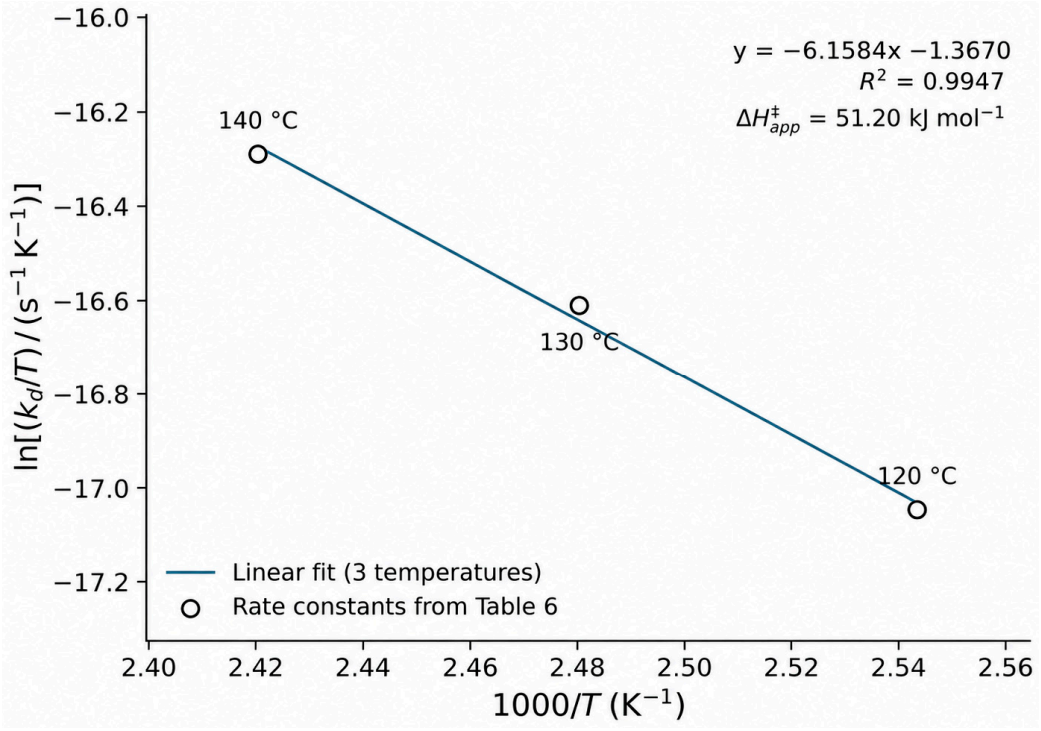

Figure 13. Arrhenius plot for the product-layer diffusion model in the linear temperature range of 120–140 °C.

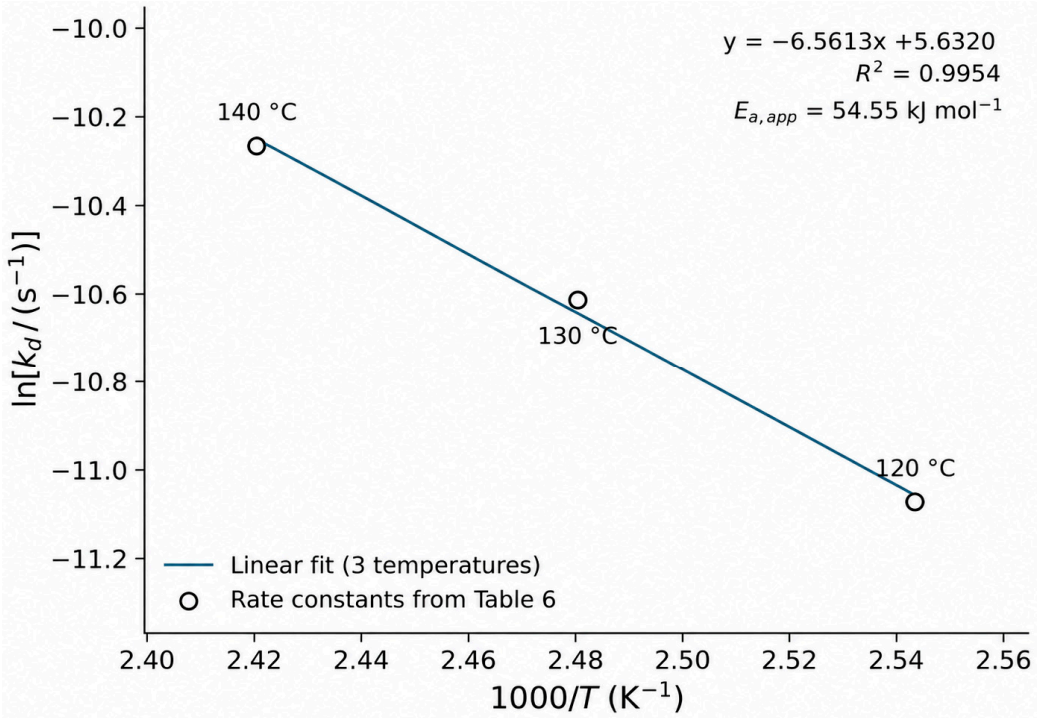

Figure 14. Eyring plot for the product-layer diffusion model in the linear temperature range of 120–140 °C.

The plot of $\ln(k_d/T)$ versus $1/T$ (Figure 14) showed a linear relationship:

$$\ln(k_d/T) = -6.1584\left(\frac{1}{T}\right) - 1.3670 \quad (20)$$

with $R^2 = 0.9947$. The corresponding activation enthalpy was positive, i.e., $\Delta H‡ = 51.2$ kJ mol^{-1}, reflecting an energetic barrier associated with the temperature-dependent leaching process [37]. The activation entropy was negative, i.e., $\Delta S‡ \approx -209$ J mol^{-1} K^{-1}, whereas the Gibbs free energy of activation remained positive at approximately 133–138 kJ mol^{-1}. The Arrhenius and Eyring parameters were derived from the same three rate constants and are therefore not independent validation results. Their relationship is consistent with the mathematical forms of the two equations. Given the limited temperature interval and the single residual degree of freedom, the Eyring parameters should be regarded as preliminary, model-dependent estimates and should not be used to infer a specific transition-state structure or rate-controlling mechanism.

3.5. Proposed Mechanism of Vanadium Leaching

The mechanism of vanadium extraction from the Balasausqandiq quartzite was interpreted by integrating the mineralogical transformations observed after leaching with the redox behavior of the system, thermodynamic calculations, and kinetic modeling. The initial ore is dominated by quartz, whereas vanadium occurs in several minor phases, including FeV_2S_4, copper vanadium sulfide, vanadian-barian muscovite, and other accessory minerals (Figure 7). Pyrite and iron hydroxides were also identified.

Under oxidative autoclave conditions, the principal redox reactions considered are summarized in Table 7.

Table 7. Thermodynamic parameters of reactions relevant to oxidative sulfuric acid leaching of vanadium-bearing quartzite calculated using HSC Chemistry.

No.	Reaction	$\Delta_r H^\circ_{140°C}$, kJ mol^{-1}	$\Delta_r G^\circ_{140°C}$, kJ mol^{-1}	Thermodynamic Implication
R1	$2FeS_2 + 7O_2 + 2H_2O \rightarrow 2FeSO_4 + 2H_2SO_4$	−2570.6	−2108.5	Strongly favorable
R2	$4FeS_2 + 15O_2 + 2H_2O \rightarrow 2Fe_2(SO_4)_3 + 2H_2SO_4$	−5539.5	−4508.3	Strongly favorable
R3	$4FeSO_4 + O_2 + 2H_2SO_4 \rightarrow 2Fe_2(SO_4)_3 + 2H_2O$	−398.2	−291.2	Favorable Fe(II) oxidation
R4	$4VO^{2+} + O_2 + 2H_2O \rightarrow 4VO_2^+ + 4H^+$	−158.9	−75.1	Favorable V(IV) oxidation by O_2
R5	$Fe^{2+} + NO_3^- + 2H^+ \rightarrow Fe^{3+} + NO_2 + H_2O$	+10.8	−1.01	Thermodynamically feasible but weakly favored
R6	$VO^{2+} + F3^{3+} + H_2O \rightarrow VO_2^+ + Fe^{2+} + 2H^+$	+63.3	+3.51	Not favorable under standard-state conditions
R7	$2NO + O_2 \rightarrow 2NO_2$	−115.5	−53.5	Favorable NO reoxidation

Note: Thermodynamic calculations were performed using HSC Chemistry for the species explicitly specified in the reaction equations. The calculated $\Delta_r H^\circ_{140°C}$ and $\Delta_r G^\circ_{140°C}$ values correspond to standard-state thermodynamic functions at the indicated temperatures and should not be interpreted as the actual Gibbs energies of the multicomponent autoclave slurry.

The oxidation of pyrite to ferrous and ferric sulfate is strongly thermodynamically favorable (Table 7, R1), with $\Delta_r G^\circ_{140°C}$ values of −2108.5 and −4508.3 kJ mol^{-1}, respectively, at 140 °C. Further oxidation of Fe(II) is also favorable (Table 7, R2), for which $\Delta_r G^\circ_{140°C} = -291.2$ kJ mol^{-1}.

The oxidation of dissolved V(IV) by molecular oxygen (Table 7, R3) is likewise thermodynamically favorable, with $\Delta_r G^\circ_{140°C} = -75.1$ kJ mol^{-1} at 140 °C. This result is consistent with the experimentally observed positive effect of oxygen pressure on vanadium extraction and with the formation of V(V)-containing pregnant leach solutions at high ORP. Under

optimized autoclave conditions, the ORP reached 700–805 mV, and vanadium extraction increased to 88.4% (Table 4).

The nitrate-assisted oxidation of Fe(II) (Table 7, R5) was only weakly favorable under standard-state conditions ($\Delta_r G^{\circ}_{140^{\circ}C} = -1.01$ kJ mol^{-1} at 140 °C), whereas reoxidation of NO by oxygen (Table 7, R7) was more favorable ($\Delta_r G^{\circ}_{140^{\circ}C} = -53.5$ kJ mol^{-1}). These results support the possible participation of nitrogen oxide species in maintaining the oxidizing environment, although the NO/NO_2 cycle was not directly verified experimentally.

In contrast, the oxidation of V(IV) by Fe(III) (Table 7, R6) gave a slightly positive $\Delta_r G^{\circ}_{140^{\circ}C} = +3.51$ kJ mol^{-1} at 140 °C. Therefore, the present thermodynamic calculations do not support Fe(III) as the principal oxidant of V(IV) under standard-state conditions; direct oxidation by O_2 appears more consistent with the experimental trends.

The mineralogical changes after leaching support the selective dissolution of the minor reactive phases, while the quartz matrix remains largely preserved. The relative quartz content increased from 96.70 to 97.40%, whereas the abundance of FeV_2S_4, iron phosphate hydroxide, and katoite decreased (Figure 10). Copper vanadium sulfide and barium silicon oxide were no longer detected after leaching, while illite and muscovite persisted. These changes indicate that the more reactive sulfide-, Fe-, Cu-, and Ca-bearing phases are preferentially removed, whereas the layered aluminosilicates and quartz are more resistant.

The SEM–EDS results provide the same overall picture: the residue remains morphologically heterogeneous, becomes relatively enriched in Si, and contains residual vanadium in localized domains rather than being uniformly distributed throughout the matrix. This suggests that incomplete extraction is associated with relatively resistant vanadium-bearing domains that remain embedded within the siliceous structure.

The kinetic results (Table 6) are consistent with this interpretation. Among the mechanistically interpretable shrinking-core models, product-layer diffusion provided the best fit ($R^2 = 0.9787$–0.9865; AARD = 3.05–4.81%), whereas the film-diffusion and surface-reaction models showed significantly poorer agreement. The Avrami–Erofeyev equation gave the best overall empirical fit but was not used for direct mechanistic assignment. The Arrhenius and Eyring analyses suggest temperature-dependent apparent kinetics over 120–140 °C; however, their common three-point basis limits parameter precision and does not independently establish the rate-controlling mechanism.

Taken together, the results support a mechanism in which readily acid-reactive and accessible mineral domains are attacked first during the atmospheric stage, while the subsequent autoclave treatment promotes oxidative dissolution of sulfide-bearing and vanadium-bearing phases and oxidation of released V(IV) to V(V). As these reactive phases are progressively removed, the remaining solid becomes increasingly enriched in quartz and persistent aluminosilicate phases. The Si-rich residual matrix may contribute to diffusional resistance, consistent with the product-layer diffusion fit; however, the available kinetic and characterization data do not establish a unique rate-controlling mechanism.

Accordingly, the probable relative dissolution sequence may be represented as follows:

Readily acid-reactive mineral components → accessible sulfide phases and V-bearing minor phases → more resistant V-bearing aluminosilicate domains → persistent illite/muscovite-associated fraction ≫ quartz-rich residual matrix.

This proposed reactivity sequence is consistent with previous studies of vanadium-bearing black shales, in which readily accessible vanadium-bearing phases are preferentially attacked, whereas vanadium structurally incorporated into mica/illite-type aluminosilicates requires progressive disruption of the aluminosilicate lattice. During pressure acid leaching, dissolution of the V-bearing aluminosilicate fraction has been reported to leave an increasingly quartz-rich residual layer, which can impose additional diffusional resistance to further vanadium extraction [22,38,39].

However, this sequence should be regarded as a proposed relative reactivity order rather than a directly measured temporal sequence because intermediate solids were not characterized separately after each leaching stage. Nevertheless, the combined XRD, SEM–EDS, kinetic, and thermodynamic results consistently indicate the selective extraction of reactive V-bearing minor phases from a largely preserved quartz-rich matrix.

4. Conclusions

A two-stage sulfuric acid leaching process combining atmospheric decarbonization–neutralization with oxidative autoclave treatment was developed for vanadium recovery from Balasausqandiq quartzite ore. The atmospheric stage was effectively performed at 90 ± 5 °C for 60 min and a solid-to-liquid ratio of 1:2, while the optimized autoclave conditions were 140 °C, 120 min, 150 kg t^{-1} H_2SO_4, 5 kg t^{-1} HNO_3, an O_2 overpressure of 3 atm, and a solid-to-liquid ratio of 1:1. Under these conditions, vanadium extraction reached 88.4%.

Mineralogical and microstructural analyses demonstrated selective dissolution of the reactive minor phases, while the quartz-rich matrix remained largely preserved. The relative quartz content increased from 96.70 to 97.40%, whereas FeV_2S_4, iron phosphate hydroxide, and katoite decreased, and the Cu–V sulfide phase was no longer detected after leaching. SEM–EDS confirmed the formation of a Si-enriched heterogeneous residue containing localized residual vanadium domains. The final sludge flux contained 72.5 wt.% SiO_2 and <0.01 wt.% carbon, suggesting potential for its further evaluation as a silica-bearing metallurgical feedstock.

Kinetic analysis revealed that, among the shrinking-core models tested, the product-layer diffusion model best fitted the available observations, suggesting a possible contribution from diffusional resistance within the silica-rich residual matrix. However, the limited number of sampling times and the absence of independent experimental replicates prevent definitive identification of the rate-controlling mechanism. Arrhenius and Eyring regressions based on three temperatures (120, 130, and 140 °C) yielded preliminary apparent estimates of E_a = 54.55 kJ mol^{-1} and ΔH‡ = 51.2 kJ mol^{-1}. Their limited statistical basis precludes strong conclusions about parameter precision or the underlying mechanism. These apparent parameters should be interpreted as model-dependent estimates whose precision remains to be established using a more extensive kinetic dataset. Thermodynamic calculations supported the oxidative mechanism: oxidation of V(IV) to V(V) by O_2 was thermodynamically favorable ($\Delta_r G^\circ = -75.1$ kJ mol at 140 °C), whereas Fe(III)-mediated V(IV) oxidation was not favored under standard-state conditions.

Overall, the results indicate that vanadium recovery proceeds through preferential dissolution of accessible reactive and V-bearing minor phases, followed by increasingly restricted extraction from more resistant aluminosilicate domains within the persistent silica-rich matrix. The proposed process combines vanadium recovery with the generation of a silica-rich residue that may serve as a secondary metallurgical feedstock. Its suitability for ferrosilicon production requires dedicated smelting tests and further technical and economic evaluation.

Supplementary Materials: The following supporting information can be downloaded at: https://www.mdpi.com/article/10.3390/ma19224808/s1, Figure S1: Enlarged schematic representation of the reactor; Figure S2: Enlarged schematic representation of the Nutsche filter; Figure S3: (a) SEM image of the initial vanadium-bearing quartzite from the Balasausqandiq deposit showing the locations of the 13 points selected for EDS analysis; (b) representative EDS spectrum acquired at analysis point 10; Figure S4: (a) SEM image of the solid residue after two-stage leaching showing the locations of the 12 points selected for EDS analysis; (b) representative EDS spectrum acquired at analysis point 23; Figure S5: Nonlinear fitting of the experimental vanadium extraction data using the film

diffusion model at 120–150 °C. Symbols represent experimental values and lines represent model predictions; Figure S6: Nonlinear fitting of the experimental vanadium extraction data using the chemical reaction control model at 120–150 °C. Symbols represent experimental values and lines represent model predictions; Figure S7: Nonlinear fitting of the experimental vanadium extraction data using the product-layer diffusion model at 120–150 °C. Symbols represent experimental values and lines represent model predictions; Figure S8: Nonlinear fitting of the experimental vanadium extraction data using the mixed control model at 120–150 °C. Symbols represent experimental values and lines represent model predictions; Figure S9: Nonlinear fitting of the experimental vanadium extraction data using the Avrami–Erofeyev model at 120–150 °C. Symbols represent experimental values and lines represent model predictions; Table S1: Average elemental composition of the initial vanadium-bearing quartzite determined by SEM–EDS point analysis (n = 12); Table S2: Average elemental composition of the solid residue after two-stage leaching determined by SEM–EDS point analysis (n = 12).

Author Contributions: D.A.: Conceptualization, Data Curation, Project Administration, Formal Analysis, Visualization, Validation, Funding Acquisition, Resources, Writing—Review & Editing. A.M.: Conceptualization, Investigation, Data Curation, Methodology, Visualization, Formal Analysis, Validation, Writing—Original Draft. A.R.: Formal Analysis, Visualization, Writing—Original Draft, Writing—Review & Editing. A.M.A.: Data Curation, Investigation, Formal Analysis, Methodology, Validation, Writing—Original Draft. All authors have read and agreed to the published version of the manuscript.

Funding: This research was funded by the Science Committee of the Ministry of Science and Higher Education of the Republic of Kazakhstan (Grant No. AP23489340, "Development of a Comprehensive Processing Technology for Vanadium-Bearing Karatau Quartzites with Ferroalloy Production").

Data Availability Statement: The original contributions presented in this study are included in the article/Supplementary Material. Further inquiries can be directed to the corresponding authors.

Conflicts of Interest: The authors declare no conflict of interest.

References

1. Yulusov, S.B.; Sarsembayeva, M.R.; Khabiyev, A.T.; Retnawati, H.; Merkibayev, Y.S.; Akbarov, M.S.; Baltabay, T.Y. Innovative Approaches to the Processing of Vanadium- and Molybdenum-Containing Technogenic Waste. *Kompleks. Ispolz. Miner. Syra = Complex Use Miner. Resour.* **2025**, *340*, 95–105. [CrossRef]
2. Ibrahim, A.H.; Lyu, X.; Sharafeldin, H.E.; ElDeeb, A.B. Eco-Friendly and Complex Processing of Vanadium-Bearing Waste for Effective Extraction of Valuable Metals and Other By-Products: A Critical Review. *Recycling* **2025**, *10*, 6. [CrossRef]
3. Nkosi, S.; Goso, X.C.; Mokone, T.; Petersen, J.; Bungane, T. Discounted Cash Flow Analysis of a Process for Vanadium Extraction from Titaniferous Slag. *Minerals* **2026**, *16*, 378. [CrossRef]
4. Liu, S.; Xue, W.; Wang, L. Extraction of the Rare Element Vanadium from Vanadium-Containing Materials by Chlorination Method: A Critical Review. *Metals* **2021**, *11*, 1301. [CrossRef]
5. Shyrokykh, T.; Volkova, O.; Sridhar, S. The Recycling of Vanadium from Steelmaking Slags: A Review. *Steel Res. Int.* **2024**, *95*, 2300477. [CrossRef]
6. Lu, Y.; Wen, J.; Mo, X.; Yang, X.; Shang, H.; Liu, X.; Sun, J.; Yang, H. Influence and Mechanism of Vanadium, Nickel, and Molybdenum Bioleaching from Black Shale by Energy Substrates. *Minerals* **2026**, *16*, 197. [CrossRef]
7. Zhumakynbai, N.; Berdikulova, F.A.; Fofanov, A.A.; Sapargalieva, G.S.; Ondiris, B.G.; Dyuskaliev, S.Z. Obtaining High-Purity Ammonium Metavanadate from Vanadium-Containing Technogenic Raw Materials Contaminated with Phosphorus and Sulfur: Integrated Technology for Solution Purification. *J. Eng. Appl. Sci.* **2026**, *73*, 94. [CrossRef]
8. Zhao, Z.; Liu, Z.; He, H.; Li, Q.; Luo, H.; Liu, W.; Lv, Y. Mechanism of Selective Extraction and Separation of Vanadium and Aluminum from Oxalic Acid Leachate of Shale: Experimental Investigation and DFT Calculations. *Separations* **2026**, *13*, 45. [CrossRef]
9. Zhao, X.; Zhang, Y.; Xue, N.; Hu, P. Research on the Mechanism of Mechanochemical Activation for Enhanced Leaching of Vanadium-Bearing Shale: Activation Kinetics and Fluorine Adsorption. *RSC Adv.* **2025**, *15*, 25233–25249. [CrossRef] [PubMed]
10. Zhao, Y.; Chen, L.; Yi, H.; Zhang, Y.; Song, S.; Bao, S. Vanadium Transitions during Roasting-Leaching Process of Vanadium Extraction from Stone Coal. *Minerals* **2018**, *8*, 63. [CrossRef]
11. Chen, F.; Zhang, Y.; Huang, J.; Liu, T.; Xue, N. Mechanism of Enhancing Extraction of Vanadium from Stone Coal by Roasting with MgO. *Minerals* **2017**, *7*, 33. [CrossRef]

12. Cai, Z.; Zhang, Y.; Liu, T.; Huang, J. Mechanisms of Vanadium Recovery from Stone Coal by Novel $BaCO_3$/CaO Composite Additive Roasting and Acid Leaching Technology. *Minerals* **2016**, *6*, 26. [CrossRef]
13. Wang, B.; Liu, T.; Zhang, Y.; Huang, J. Effect of CaF_2/CaO Composite Additive on Roasting of Vanadium-Bearing Stone Coal and Acid Leaching Kinetics. *Minerals* **2017**, *7*, 43. [CrossRef]
14. Zhang, H.; Shi, J.; Chen, C.; Yang, M.; Lu, J.; Zhang, B. Heterotrophic Bioleaching of Vanadium from Low-Grade Stone Coal by Aerobic Microbial Consortium. *Int. J. Environ. Res. Public Health* **2022**, *19*, 13375. [CrossRef] [PubMed]
15. Yuan, Y.; Zhang, Y.; Liu, T.; Chen, T. Microwave Roasting with Size Grading Based on the Influence of Carbon on Vanadium Extraction from Stone Coal via Microwave Roasting-Acid Leaching. *RSC Adv.* **2017**, *7*, 1387–1395. [CrossRef]
16. Tang, Y.; Ye, G.; Zuo, Q. Vanadium Extraction from the Flotation Concentrate of Vanadium-Bearing Shale by Process of Non-Roasting Enhanced Acid Leaching and Thermodynamics. *Molecules* **2023**, *28*, 2706. [CrossRef] [PubMed]
17. Li, X.; Wei, C.; Deng, Z.; Li, C.; Fan, G.; Li, M.; Huang, H. Recovery of Vanadium from H_2SO_4-HF Acidic Leaching Solution of Black Shale by Solvent Extraction and Precipitation. *Metals* **2016**, *6*, 63. [CrossRef]
18. Zhang, J.; Xue, N.; Zhang, Y.; Zheng, Q. High-Efficiency Stepped Separation and Recoveries of Vanadium and Molybdenum via Low-Temperature Carbonation Conversion of High-Chromium Vanadium Residue. *Processes* **2023**, *11*, 470. [CrossRef]
19. Badikova, A.; Shevko, V.; Aitkulov, D. Thermodynamic Model and Electric Smelting of a Mixture of Cake from Leaching of Vanadium-Containing Quartzites with Coal Beneficiation Tailings. *Metall. Res. Technol.* **2025**, *122*, 115. [CrossRef]
20. Shevko, V.; Badikova, A.; Mirkayev, N.; Mustafa, T. Laboratory-Scale Production of Ferrosilicon Using Amorphous Siliceous Sedimentary Rocks. *E3S Web Conf.* **2025**, *646*, 00026. [CrossRef]
21. Yessengaliyev, D.; Kelamanov, B.; Zayakin, O.; Sariyev, O.; Mikhailova, L.; Zhuniskaliyev, T.; Kuatbay, Y.; Nurgali, N.; Abikenova, G.; Abdirashit, A.; et al. Application of a Complex Si–Al–Fe Reducing Agent for the Production of a Nickel-Containing Alloy. *Sci. Rep.* **2026**, *16*, 14856. [CrossRef] [PubMed]
22. Li, M.; Wei, C.; Qiu, S.; Zhou, X.; Li, C.; Deng, Z. Kinetics of Vanadium Dissolution from Black Shale in Pressure Acid Leaching. *Hydrometallurgy* **2010**, *104*, 193–200. [CrossRef]
23. Li, M.T.; Wei, C.; Zhou, X.J.; Qiu, S.; Deng, Z.G.; Li, X.B. Kinetics of Vanadium Leaching from Black Shale in Non-Oxidative Conditions. *Miner. Process. Extr. Metall.* **2012**, *121*, 40–47. [CrossRef]
24. Xue, N.; Zhang, Y.; Liu, T.; Zheng, Q. Efficient Separation of Black Shale-Hosted Vanadium Induced by Formation of Kalunite-Jarosite Solid Solution in Two-Stage Pressurized Acid Leaching Coupled with Lixivium Recycling. *Sep. Purif. Technol.* **2021**, *269*, 118762. [CrossRef]
25. Zhao, X.; Zhang, Y.; Xue, N.; Hu, P.; Zheng, Q. Effect of H_3PO_4 Coordination on Vanadium Extraction and Iron Separation in a H_2SO_4 Leaching System. *RSC Adv.* **2024**, *14*, 37404–37418. [CrossRef] [PubMed]
26. Wu, J.; Xiao, L.; Shen, L.; Ran, J.-J.; Zhong, H.; Zhu, Y.-R.; Chen, H. Recent Advancements in Hydrometallurgical Recycling Technologies of Spent Lithium-Ion Battery Cathode Materials. *Rare Met.* **2024**, *43*, 879–899. [CrossRef]
27. Russo, V.; Grénman, H.; Cogliano, T.; Tesser, R.; Salmi, T. Advanced Shrinking Particle Model for Fluid-Reactive Solid Systems. *Front. Chem. Eng.* **2020**, *2*, 577505. [CrossRef]
28. De Bruijn, T.J.W.; De Jong, W.A.; Van Den Berg, P.J. Kinetic Parameters in Avrami—Erofeev Type Reactions from Isothermal and Non-Isothermal Experiments. *Thermochim. Acta* **1981**, *45*, 315–325. [CrossRef]
29. Eyring, H. The Activated Complex in Chemical Reactions. *J. Chem. Phys.* **1935**, *3*, 107–115. [CrossRef]
30. Андреев, С.Е.; Перов, В.А.; Зверевич, В.В. *Дробление, Измельчение и Грохочение Полезных Ископаемых (Crushing, Grinding and Screening of Minerals)*; Недра: Moscow, Russia, 1980.
31. Ali, A.; Chiang, Y.W.; Santos, R.M. X-Ray Diffraction Techniques for Mineral Characterization: A Review for Engineers of the Fundamentals, Applications, and Research Directions. *Minerals* **2022**, *12*, 205. [CrossRef]
32. Gharrabi, M.; Velde, B.; Sagon, J.-P. The Transformation of Illite to Muscovite in Pelitic Rocks: Constraints from X-Ray Diffraction. *Clays Clay Miner.* **1998**, *46*, 79–88. [CrossRef]
33. Rakhym, A.B.; Seilkhanova, G.A.; Mastai, Y. Physicochemical Evaluation of the Effect of Natural Zeolite Modification with Didodecyldimethylammonium Bromide on the Adsorption of Bisphenol-A and Propranolol Hydrochloride. *Microporous Mesoporous Mater.* **2021**, *318*, 111020. [CrossRef]
34. Xu, H.; Wei, C.; Li, C.; Fan, G.; Deng, Z.; Li, M.; Li, X. Sulfuric Acid Leaching of Zinc Silicate Ore under Pressure. *Hydrometallurgy* **2010**, *105*, 186–190. [CrossRef]
35. Vyazovkin, S.; Wight, C.A. Kinetics in Solids. *Annu. Rev. Phys. Chem.* **1997**, *48*, 125–149. [CrossRef] [PubMed]
36. Taylor, C.J.; Seki, H.; Dannheim, F.M.; Willis, M.J.; Clemens, G.; Taylor, B.A.; Chamberlain, T.W.; Bourne, R.A. An Automated Computational Approach to Kinetic Model Discrimination and Parameter Estimation. *React. Chem. Eng.* **2021**, *6*, 1404–1411. [CrossRef] [PubMed]
37. Schaleger, L.L.; Long, F.A. Entropies of Activation and Mechanisms of Reactions in Solution. In *Advances in Physical Organic Chemistry*; Gold, V., Ed.; Academic Press: New York, NY, USA, 1963; Volume 1, pp. 1–33.

38. Xue, N.; Zhang, Y.; Liu, T.; Huang, J.; Zheng, Q. Effects of Hydration and Hardening of Calcium Sulfate on Muscovite Dissolution during Pressure Acid Leaching of Black Shale. *J. Clean. Prod.* **2017**, *149*, 989–998. [CrossRef]
39. Lu, Y.-H.; Wen, J.-K.; Mo, X.-L.; Yang, X.-L.; Gao, W.-C.; Yang, H.-Y. A Review of Mechanism and Technology of Vanadium Extraction from Strategic Mineral Black Shale. *Rare Met.* **2024**, *43*, 6183–6200. [CrossRef]

Disclaimer/Publisher's Note: The statements, opinions and data contained in all publications are solely those of the individual author(s) and contributor(s) and not of MDPI and/or the editor(s). MDPI and/or the editor(s) disclaim responsibility for any injury to people or property resulting from any ideas, methods, instructions or products referred to in the content.